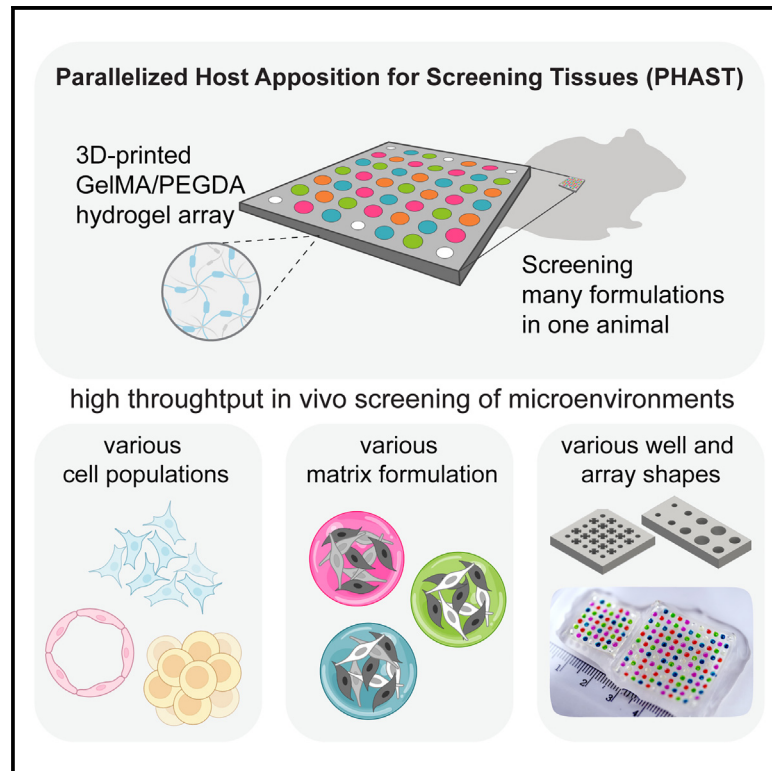


## Bioprinted platform for parallelized screening of engineered microtissues *in vivo*

### Graphical abstract



### Authors

Colleen E. O'Connor, Fan Zhang, Anna Neufeld, ..., Elizabeth C. Wayne, Daniela M. Witten, Kelly R. Stevens

### Correspondence

ksteve@uw.edu

### In brief

O'Connor, Zhang, Stevens, and colleagues present PHAST, a powerful high-throughput platform that enables *in vivo* screening of 43 engineered tissues within a single animal. PHAST enables rapid identification of cellular and material formulations that support tissue vascularization and engraftment *in vivo*, paving the way for next-generation therapeutic tissues for regenerative medicine.

### Highlights

- PHAST enables parallelized *in vivo* testing of 43 microtissues in one device
- PHAST identifies tissue formulations for vascular inosculation and hepatocyte implant
- This platform accelerates development of tissue engineering and regenerative medicine



## Technology

# Bioprinted platform for parallelized screening of engineered microtissues *in vivo*

Colleen E. O'Connor,<sup>1,2,9</sup> Fan Zhang,<sup>1,2,9</sup> Anna Neufeld,<sup>3</sup> Olivia Prado,<sup>1,2</sup> Susana P. Simmonds,<sup>1,2</sup> Chelsea L. Fortin,<sup>1,2,4</sup> Fredrik Johansson,<sup>1,2</sup> Jonathan Mene,<sup>1,2</sup> Sarah H. Saxton,<sup>1,2</sup> Irina Kopyeva,<sup>1</sup> Nicole E. Gregorio,<sup>1</sup> Zachary James,<sup>1</sup> Cole A. DeForest,<sup>1,2,5</sup> Elizabeth C. Wayne,<sup>1,2</sup> Daniela M. Witten,<sup>3,6</sup> and Kelly R. Stevens<sup>1,2,4,7,8,10,\*</sup>

<sup>1</sup>Department of Bioengineering, University of Washington, Seattle, WA 98195, USA

<sup>2</sup>Institute for Stem Cell and Regenerative Medicine, Seattle, WA 98195, USA

<sup>3</sup>Department of Statistics, University of Washington, Seattle, WA, USA

<sup>4</sup>Department of Laboratory Medicine & Pathology, University of Washington, Seattle, WA 98195, USA

<sup>5</sup>Department of Chemical Engineering, University of Washington, Seattle, WA 98195, USA

<sup>6</sup>Department of Biostatistics, University of Washington, Seattle, WA, USA

<sup>7</sup>Center for Cardiovascular Biology, University of Washington, Seattle, WA 98195, USA

<sup>8</sup>Brotman Baty Institute, Seattle, WA 98195, USA

<sup>9</sup>These authors contributed equally

<sup>10</sup>Lead contact

\*Correspondence: [ksteve@uw.edu](mailto:ksteve@uw.edu)

<https://doi.org/10.1016/j.stem.2025.03.002>

## SUMMARY

Human engineered tissues hold great promise for therapeutic tissue regeneration and repair. Yet, development of these technologies often stalls at the stage of *in vivo* studies due to the complexity of engineered tissue formulations, which are often composed of diverse cell populations and material elements, along with the tedious nature of *in vivo* experiments. We introduce a “plug and play” platform called parallelized host apposition for screening tissues *in vivo* (PHAST). PHAST enables parallelized *in vivo* testing of 43 three-dimensional microtissues in a single 3D-printed device. Using PHAST, we screen microtissue formations with varying cellular and material components and identify formulations that support vascular graft-host inosculation and engineered liver tissue function *in vivo*. Our studies reveal that the cellular population(s) that should be included in engineered tissues for optimal *in vivo* performance is material dependent. PHAST could thus accelerate development of human tissue therapies for clinical regeneration and repair.

## INTRODUCTION

Human engineered tissues and other cellular and material-based technologies hold enormous potential for treating a vast spectrum of human disease. Over the past several decades, a massive portfolio of such technologies has been developed for diverse purposes,<sup>1</sup> such as replacing or supplementing the functions of tissues and organs,<sup>1–5</sup> promoting angiogenesis,<sup>6–10</sup> promoting transplanted cell survival<sup>11–14</sup> or fate choice,<sup>15,16</sup> modulating the immune response,<sup>17–19</sup> capturing malignant cells,<sup>20</sup> or delivering biological therapeutics.<sup>21–23</sup>

Many of these technologies have multiple components that are both living and synthetic. Human engineered tissues, for example, are typically composed of at least one and often multiple human cellular population(s) embedded within highly engineered synthetic or natural biomaterials.<sup>24–28</sup> The choice on which cellular population(s) and biomaterial components to include, and even the relative ratios between multiple cell types or materials, is ultimately determined after iterative experimentation.

*In vivo* studies remain essential to this experimentation process, as host-mediated biological processes interact with both

transplanted cells and materials to determine a technology's outcome.<sup>29,30</sup> Host-mediated processes impact transplanted cell survival, integration of grafted engineered tissues with host vasculature, immune response to implanted materials, absorption, distribution, metabolism, and excretion of therapeutic agents, and more. Many technologies even rely upon host biology to enhance their therapeutic outcome.<sup>31–38</sup> In each of these cases, the outcome depends on the material or cellular formulation of the implant.<sup>20,39–41</sup>

Our incomplete understanding of the “black box” of such host-mediated processes means that each material and cell formulation must be tested empirically *in vivo*. The sheer number of material and cellular permutations possible, together with the low-throughput nature of animal experiments, in which a single or at most a few implant(s) is typically implanted into a given host, has meant progress slows to a crawl at the stage of *in vivo* studies (Figure 1A).<sup>40,41</sup> New methods that overcome this time, financial, and ethical bottleneck would massively accelerate regenerative engineering and medicine.<sup>30,42–44</sup>

At the stage of *in vitro* studies, previous progress in miniaturizing biological assays, such as advancements in multiwell



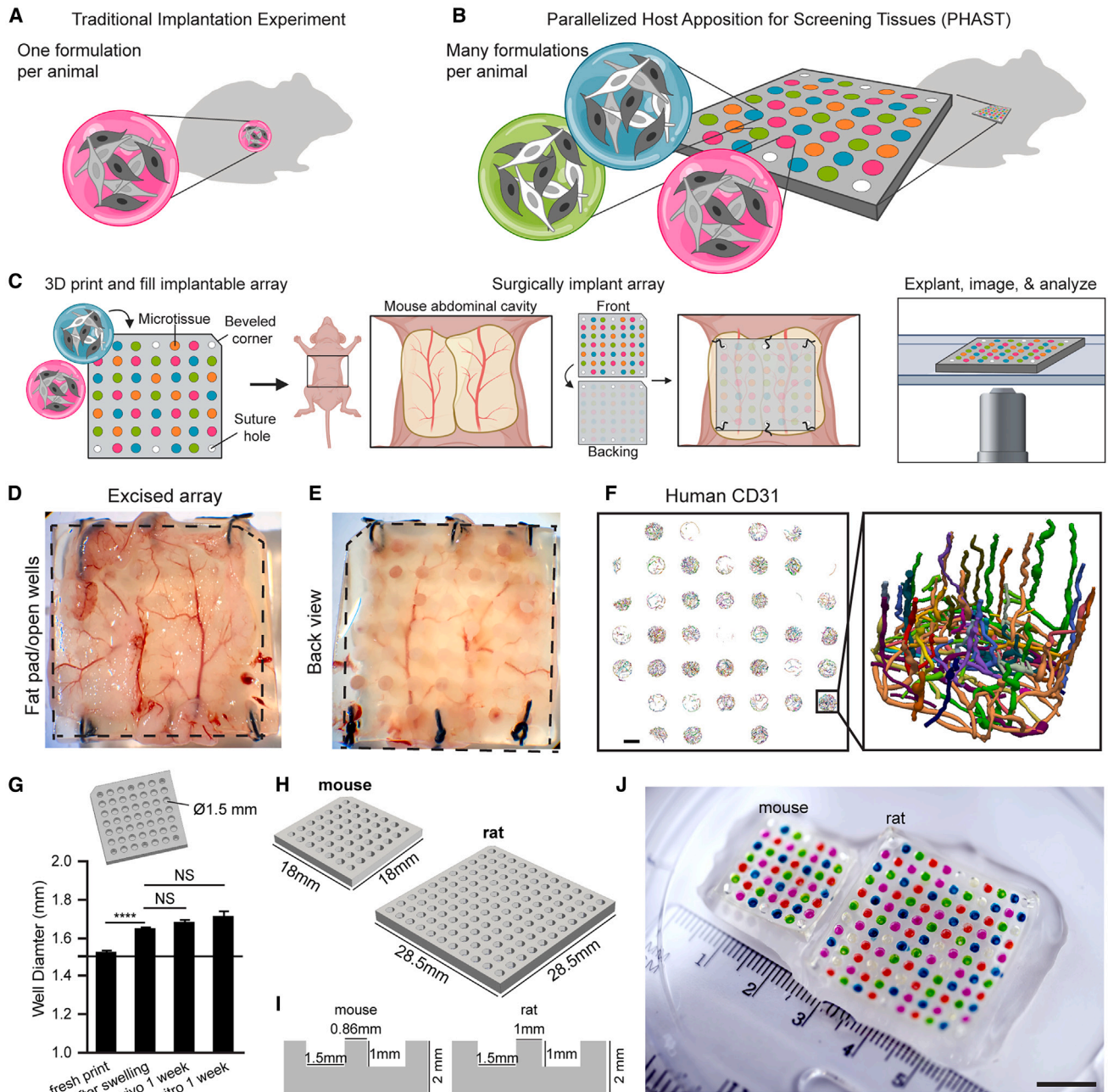


**Figure 1. Development of PHAST for *in vivo* screening**

(A) A traditional *in vivo* experiment where only one formulation is typically tested in an animal host.

(B) PHAST platform, in which many material and/or cellular formulations are screened in parallel within a single animal host.

(C) PHAST workflow depicting 3D printing and filling PHAST array (left); surgically implanting array into abdominal space of mouse host (center); and explanting, imaging, and analyzing array in 3D (right).

(D and E) (D) Front and (E) back views of an explanted PHAST device after 1 week *in vivo*, demonstrating the host fat pad adhered across the top of the open wells of the array.

(F) (Left) PHAST array with 3D reconstructed self-assembled vascular networks (huCD31<sup>+</sup>) within each microwell. Scale bar, 1 mm. (Right) Angled orientation of a single microwell showing a 3D reconstructed network. Individual colors represent individually segmented microvessels. The angled view indicates human endothelial vessels protruding up and away from the microwell bottom.

(G) (Top) CAD design of PHAST device sized for mouse. Designed diameter ( $\emptyset$ ) of each microwell is 1.5 mm. (Bottom) Well diameter increases after swelling but then remains stable in mouse or *in vitro* culture for 1 week. Horizontal line indicates  $\emptyset$ . Data are represented as mean  $\pm$  SEM. \*\*\*\* $p < 0.0001$  by one-way ANOVA followed by Tukey's post hoc test. NS, no significant difference.

(H and I) (H) CAD designs and (I) cross sections of PHAST device sized for mouse and rat.

(J) Printed mouse and rat PHAST array with a variety of different fillings. Scale bar, 1 cm.

plates, robotic liquid handling, microarray technology, and microfabrication ushered in a new era of parallelized and combinatorial screening.<sup>45–50</sup> We postulated that analogous approaches for screening material- and cell-based technologies such as engineered tissues at the *in vivo* stage of product development could accelerate pre-clinical progress.

Here, we introduce a new method for parallelized host apposition for screening tissues (PHAST) to interrogate material- and cell-based tissue environments *in vivo* at scale (Figure 1B). This method adapts 3D printing technology to fabricate implantable arrays with individually addressable material- and cell-based tissue environments (Figure 1B). We use PHAST to uncover how the combinatorial material- and cell-based environments govern vascular graft-host inosculation and liver tissue function within implanted engineered tissues *in vivo*.

## DESIGN

We recently developed a stereolithography apparatus for tissue engineering (SLATE), which enabled 3D printing of biocompatible hydrogels to create complex topologies volumetrically by converting photoactive liquids into structured parts through localized photopolymerization.<sup>51</sup> We identified photopolymerizable hydrogel formulations that can be 3D printed using SLATE to create engineered tissues, which could be successfully implanted in animals for several weeks.<sup>51</sup> We reasoned that this 3D printing technology could alternatively be leveraged for rapid fabrication of biocompatible devices for *in vivo* screening.

Toward this end, we sought to design a 3D-printed PHAST device with individually addressable wells for parallelized and combinatorial screening that can be implanted *in vivo* (Figures 1C–1E). In this device, each individually addressable well could be filled with different material- and cell-based formulations, which can be retained in the device after implantation for downstream analyses, such as biomedical imaging (Figure 1C). Formulations in each well would comprise any user-defined combination of materials (e.g., hydrogels and extracellular matrices), cellular composition (e.g., cell type(s), density, and ratio), or biological molecules. Since these studies use both material and cellular components, we will henceforth call the formulations within each well of the PHAST device “microtissues” (Figure 1F).

We arrived at the final PHAST device design (Figure 1) after a series of prototype iterations. During this iteration process, we imposed design constraints upon the PHAST device as follows: the device should (1) retain its structural integrity (i.e., not break or crack) throughout the experiment, (2) remain pliable and hydrated to facilitate apposition with host tissue even with host movement after implantation, (3) minimize or eliminate potential crosstalk or interactions between wells within the device, and (4) facilitate downstream analyses such as histology.

To achieve these goals, we first sought to identify a biocompatible photopolymerizable hydrogel material for device fabrication that retains its structural integrity, remains pliable, prevents cellular infiltration between wells, and can be readily sectioned. We settled upon gelatin methacrylate (GelMA, 10 weight % [wt %]), and poly(ethylene glycol) diacrylate (PEGDA, 3.4 kDa, 3.25 wt %) because inclusion of PEGDA imparts mechanical strength to the hydrogel,<sup>52,53</sup> inhibits degradation, and prevents cellular infiltration between wells, while inclusion of GelMA facil-

itates host apposition and subsequent downstream analysis techniques such as tissue sectioning.<sup>54–58</sup>

We next leveraged the rapid prototyping capabilities of SLATE to iterate through early prototypes of different device architectural (topology) designs (Figure S1A). In early prototyping studies, we created several potential PHAST designs using computer-aided design (CAD) and then 3D printed the devices using SLATE.<sup>51</sup>

For example, we designed and tested an early device architecture containing an array of nine cylindrical wells, each with a diameter of 3 mm, that were open on both faces, such that microtissues and host tissue were directly apposed on both sides of the device upon implantation (Figure S1A, left). To test this array prototype, we filled the wells of the array with a fibrin hydrogel and then surgically implanted the prototype on perigonadal adipose tissue in the abdominal space of an athymic mouse. Upon explant after 1 week, we found that host tissues (i.e., intestine) frequently protruded through the wells in this open-well system, dislodging microtissues from the array and prohibiting downstream analysis on microtissues (Figure S1B).

To overcome this obstacle, we added a backing component to the design, essentially creating a hydrogel “well plate,” wherein each cylindrical well comprises one open face (Figure S1A, right). This design enabled microtissues to directly interface with host tissue on one side, while the closed side prevented host tissue penetration through the array. The rapid fabrication capabilities of SLATE enabled us to also adjust both the shape and size of individual wells (Figure 1G vs. Figure S1C, cylindrical vs. X-shaped wells), as well as the overall dimensions of the array to fit within different animal models (Figures 1H–1J), which were similarly tested in *in vitro* or *in vivo* pilot studies.

Ultimately, we settled on a final PHAST array design in which wells were cylindrical in shape and 1.5 mm diameter in size (Figures 1G and 1H). This well dimension enabled us to scale the number of wells per array to 43 wells or 115 wells for arrays designed to be implanted in mice and rats, respectfully (Figures 1H–1J). The distance between wells was kept >0.85 mm to minimize potential paracrine interactions between wells (Figure 1I). Finally, we added a beveled edge to the top-right corner to define device orientation and open wells (no backing) at the corners and center of array edges for suturing the array to host tissue (Figures 1G–1J).

The PHAST array designed for mouse studies was used for the rest of the studies here (Figure 1G). This PHAST array contains a grid of 7 by 7 wells, to make 43 individual microtissue wells with backing and 6 open suture holes (Figures 1G–1J). Each array is 3D printed in minutes and then incubated in phosphate-buffered saline (PBS) to enable the network hydrogel to reach equilibrium (“swell”) and diffuse out tartrazine used for printing. Freshly printed arrays have an average microwell diameter of  $1.52 \pm 0.01$  mm. Microwell diameter increases slightly to  $1.65 \pm 0.01$  mm after incubation in PBS for 24 h (Figure 1G). After this initial swelling period, we observed no further significant changes in microwell diameter, array dimensions, or structural fidelity after an additional incubation *in vitro* or *in vivo* (Figure 1G).

After fabrication and swelling, the microtissue wells can then be filled via standard pipetting. This design supports robust engraftment, as visualized by direct apposition of the perigonadal fat pad to the array after explant of the PHAST array from the mouse host (Figures 1D and 1E). Each well within the

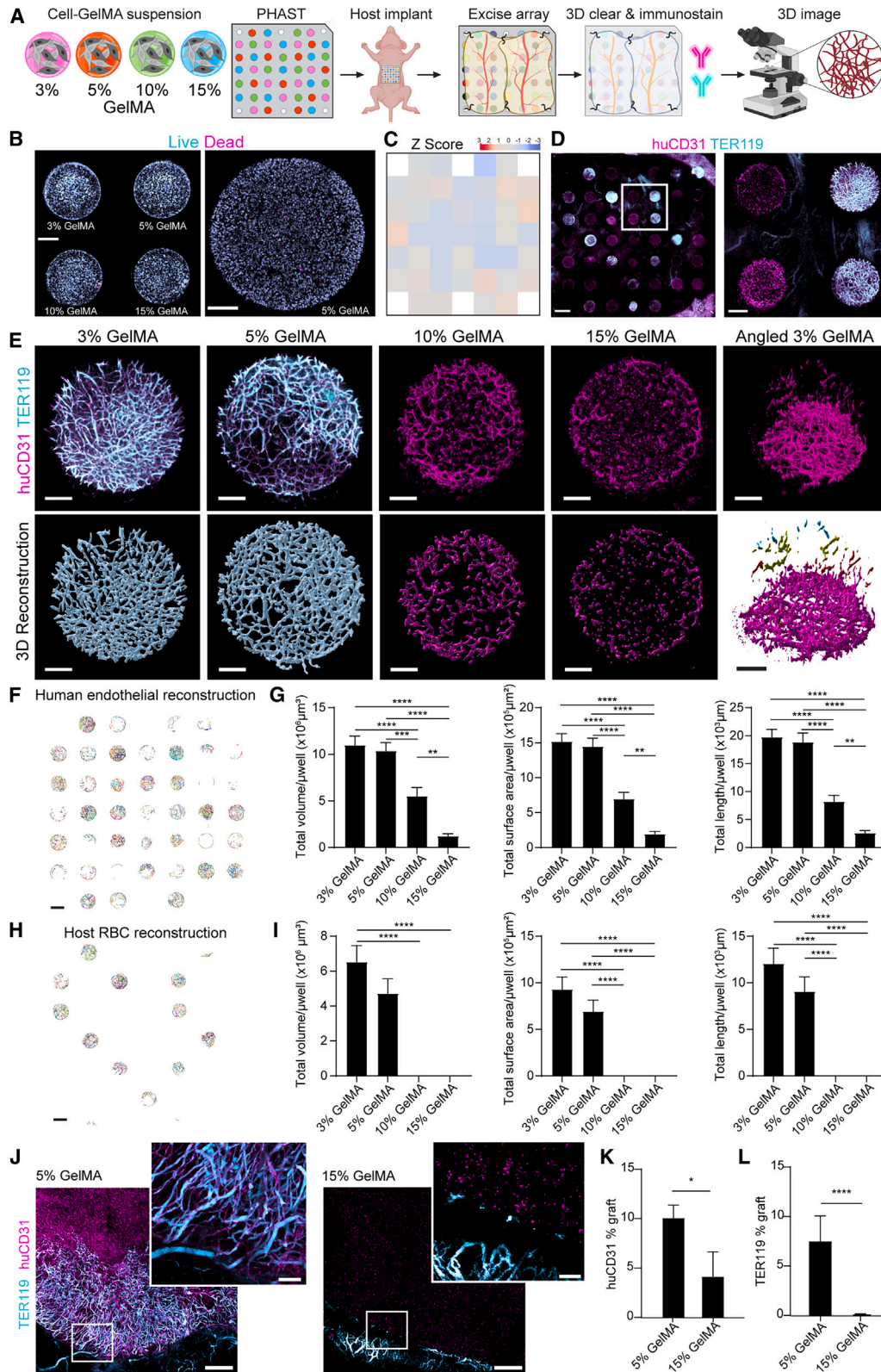


**Figure 2. PHAST identifies material microenvironments that support vascular assembly *in vivo***

(A) Experimental design and workflow, which assessed 4 different GelMA formulations, each having 11 technical replicates per animal. Mice  $n = 4$ , each receiving the same array layout.

(legend continued on next page)

explanted arrays can then be cleared, immunostained, imaged in 3D, and computationally analyzed.<sup>59</sup> Here, computational reconstructions of the PHAST array (Figure 1F, left) and insets of a given well (Figure 1F, right) show how PHAST array design guides human endothelial cells to form networks that reach upward within the wells to inosculate (connect) with the host, as opposed to across or between wells (Figure 1F). This PHAST design thus opens the possibility of testing up to 43 different material- and cell-based microtissue formulations in a single mouse.

## RESULTS

### Screening material microenvironments for vascular assembly *in vivo*

To demonstrate the utility of PHAST, we first focused our attention on vascularization of engineered tissues, which remains a major unsolved challenge for building solid tissues and organs for therapeutic transplant.<sup>32,51,60–63</sup> We focused on graft-host vascular inosculature, which involves seeding endothelial cells and sometimes stromal cells in an engineered tissue that then self-assemble *in vitro* to form a vascular network, which is not yet perfused. Upon implantation of the engineered tissue *in vivo* into a host, the host blood vessels self-organize to connect—or “inosculate”—with the pre-assembled graft network in the engineered tissue, filling the network with host blood.

Since this process is required for the grafted vessels to carry blood that metabolically supports the engineered tissue, it relies upon successful *in vivo* implantation and robust inosculature between graft and host.<sup>64–68</sup> Importantly, the fidelity of graft-host vascular inosculature depends on the formulation of the implant.<sup>20,39</sup> Many biomaterials, including numerous “bioinks” commonly used for 3D printing engineered tissues and organs, do not robustly support this process. Here, we thus sought to demonstrate utility of PHAST by screening different material bioinks for stereolithography (SLA)-based bioprinting for their capacity to support vascular inosculature *in vivo* (Figure 2A).

We focused our studies on GelMA, a widely used SLA bioink that is biocompatible,<sup>69</sup> cost effective, has bioactive moieties that support cell attachment,<sup>70</sup> and has photoactive moieties that facilitate its usage with numerous biofabrication strategies,<sup>71–73</sup> including 3D printing.<sup>74</sup> We suspended endothelial cells (primary human um-

bilical vein endothelial cells [HUVECs]) and stromal cells (primary normal human dermal fibroblasts [NHDFs]) within 3, 5, 10, or 15 wt % GelMA bioinks, which represent a range of material properties (Figure S1D). We first performed *in vitro* studies and found that these bioinks supported vascular assembly *in vitro* in a dose-dependent fashion (Figure S2A), with 3% and 5% GelMA supporting most and 15% GelMA supporting negligible vascular assembly.

To further assess the extent to which each material could support the graft networks to inosculate with host vasculature and become filled with blood, we used PHAST. To do this, we dispensed the same GelMA pre-polymers cellularized with human vascular cells into PHAST wells to form microtissues in a randomized manner across the array (Figure 2A). In these early studies, we intentionally screened only four GelMA formulations, each with 10–11 technical replicates across the array, for a characterization experiment that could be leveraged to identify optimal array layouts and statistical power. After filling, the entire PHAST array was exposed to violet light (405 nm) to polymerize the cellularized GelMA microenvironments within the array wells.<sup>75,76</sup> After filling and polymerization, a majority of cells within all GelMA microenvironments remained viable (Figure 2B). Z scores were computed for number of viable cells in each microwell. All wells have Z scores less than 2, suggesting similar initial number of living cells across the array (Figure 2C).

The filled PHAST arrays were then surgically implanted onto the perigonadal fat pad of athymic mice (Figure 2A). After 1 week *in vivo*, arrays were excised and cleared to render the PHAST array transparent and optically clear, to permit deeper imaging.<sup>77</sup> Cleared arrays were then 3D immunostained for human endothelial cells (huCD31, magenta) and mouse red blood cells (RBCs, TER119, cyan) (Figures 2D and 2E). Here, magenta huCD31 signal thus serves as a proxy for human vascular network self-assembly, and cyan TER119 signal serves as a proxy for graft-host inosculature, as evidenced by the extent to which vascular networks become filled with host blood after inosculature. Subsequent 3D image analysis of immunostained arrays revealed a range of self-assembled and blood-filled human endothelial networks within the various wells (Figures 2E–2I and S2C–S2G).

To parameterize and quantify huCD31<sup>+</sup> and TER119<sup>+</sup> across arrays (Figures 2F–2I), we leveraged network reconstruction

(B) PHAST wells with HUVECs in 3%–15% GelMA and stained for live (calcein, cyan) and dead (ethidium homodimer, magenta) cells. Scale bars, 400  $\mu$ m (left) and 200  $\mu$ m (right).

(C) Z score of living cell count across the PHAST array.

(D) (Left) An explanted PHAST device immunostained with huCD31 (human endothelial cells; magenta) and TER119 (mouse RBCs; cyan) after 1 week *in vivo*. Scale bars, 1,500  $\mu$ m. (Right) Magnification inset of four microwells. Scale bars, 400  $\mu$ m.

(E) Representative microtissues stained for human CD31 (magenta) and mouse TER119 (cyan) representing the four microenvironments screened: 3% GelMA, 5% GelMA, 10% GelMA, and 15% GelMA. Scale bars, 200  $\mu$ m.

(F) Reconstructed human CD31<sup>+</sup> microvascular networks across an explanted PHAST array. Scale bar, 1 mm.

(G) HuCD31<sup>+</sup> network volume, surface area, and total length per microwell for each microenvironment screened. \*\*\*\* $p < 0.0001$ , \*\*\* $p < 0.001$ , \*\* $p < 0.01$  by one-way ANOVA followed by Tukey's post hoc test.

(H) Reconstructed mouse TER119<sup>+</sup> inosculated networks across an explanted PHAST array. Scale bar, 1 mm.

(I) TER119<sup>+</sup> network volume, surface area, and total length per microwell for each microenvironment screened. \*\*\*\* $p < 0.0001$  by one-way ANOVA followed by Tukey's post hoc test.

(J) Larger-scale discrete engineered tissues made from 5% GelMA (left) and 15% GelMA (right) stained by huCD31 (magenta) and TER119 (cyan) after 1 week *in vivo*. Scale bars, low magnification: 1 mm; high magnification inset: 100  $\mu$ m.

(K) HuCD31<sup>+</sup> area percentage to total tissue graft area.

(L) TER119<sup>+</sup> area percentage to total tissue graft area.  $n = 7$ . \*\*\*\* $p < 0.0001$ , \* $p < 0.05$  by Mann-Whitney test. All data are represented as mean  $\pm$  SEM.

and visualization software. Similar to our *in vitro* results, we identified a dose-dependent inverse relationship between endothelial cell network assembly and GelMA material weight percentage (Figure 2G), with a 13-fold difference in assembled network volume between the lowest and highest wt % GelMA conditions (Figures 2E–2G and S2E). However and interestingly, only 3 and 5 wt % GelMA microenvironments had vascular networks that also contained mouse RBCs, suggesting successful inosculation of only these networks with the host vasculature (Figures 2E, 2H, and S2F). The 10 and 15 wt % GelMA microenvironments were mostly void of RBCs (Figures 2E and 2H). These results were validated with 2D histological analyses, which demonstrated that 3 and 5 wt % GelMA microenvironments contained microvascular structures filled with RBCs. Conversely, 10 wt % microenvironments had sparse microvascular structures with no blood, and 15 wt % microenvironments contained only punctate cells, again with no blood (Figures S2H–S2K). Thus, vascular self-assembly *in vitro* alone did not accurately predict which materials supported networks to become inosculated with host vasculature and become filled with host blood *in vivo*.

Although the array device in these studies was composed predominantly of PEGDA, a relatively inert biomaterial, we had also included some GelMA in the array device to improve graft-host apposition as well as the capacity for arrays to be sectioned for histology after explant. It is possible that the presence of bioactive cues in GelMA could affect the biological results of PHAST screening. To assess this possibility, we conducted an experiment that replicated the experimental design of Figure 2, only used PHAST arrays composed only of 13.25 wt % PEGDA without GelMA (Figure S3). The results from the PEGDA-only arrays closely mirrored those from the regular PHAST array, suggesting that the inclusion of GelMA does not impact the overall results of the experiment (Figure S3). Notably, we found empirically that PEGDA-only arrays were more challenging to surgically implant and handle. For example, ripping of the suture holes was common upon implantation, and the arrays could not readily be sectioned for 2D histological analysis after explant. Thus, for the remaining PHAST studies in this manuscript we used arrays with a 10% GelMA/3.25% PEGDA array formulation.

Finally, we validated PHAST findings using discrete 3D-printed engineered tissues of much larger size (centimeter scale) that were each implanted into separate mice. This validation study was important because prior work has shown that tissue shape and size can impact cellular behavior within engineered tissues, and systemic responses to one condition could in theory impact all conditions.<sup>78–80</sup> We thus fabricated disc-shaped engineered tissues that were ~18 mm in diameter and ~1 mm thick, both from 5% or 15% GelMA hydrogel and containing vascular cells embedded across the tissue bulk, similar to formulations from PHAST studies above. After 7 days of implantation, we found that, similar to PHAST studies, 5% GelMA supported substantive self-assembly of human vessel networks as well as successful graft-host inosculation, as indicated by the presence of host (mouse) blood in these networks (Figure 2J). This inosculation was especially evident within ~2 mm of the tissue edge, as expected for a phenomenon reliant on graft-host integration (Figure 2J). An example of a graft-host inosculation point is directly visualized in the inset of panel Figure 2J (left), showing a host

vessel (lower left) integrating with the human vascular network and supplying blood to graft-derived vessels (upper right). 15% GelMA supported some but less vascular self-assembly compared with 5% GelMA (Figures 2J and 2K). However and importantly, although 15% GelMA did support some self-assembly, these networks did not become filled with host blood and no graft-host vascular connections could be found, indicating inosculation was not successful (Figures 2J and 2L; inset shows graft-host interface area). Thus, PHAST accurately predicted results for bioprinted tissues of more scaled size implanted into discrete mice.

Taken together, PHAST allowed us to show that human vascular network self-assembly and inosculation with the host *in vivo* heavily depends upon formulation of the microenvironment that encases the grafted endothelial cells. Furthermore and importantly, PHAST identified microenvironments such as 10% and 15% GelMA, both of which are routinely used for bioprinting,<sup>81–85</sup> that supported vascular self-assembly *in vitro* but not inosculation to host vessels *in vivo*.

#### A PHAST device that overcomes potential position effects and crosstalk

While our initial study (Figure 2) demonstrated the utility of PHAST, we next sought to increase the impact of PHAST for parallelized screening by increasing the number of conditions tested per animal. Testing more conditions per animal reduces the number of technical replicates per array, which exacerbates the possibility that the technical replicates corresponding to a particular condition might be located in a small area of the array, leading to results that are confounded by a “position effect.” That is, spatial variability of host features in the animal tissue (e.g., branching large vessels) or variable host tissue apposition across an array could affect the experimental outcome. Thus, we set out to further develop the PHAST platform to protect against this position effect.

To do this, we designed a set of array layouts to ensure that every experimental condition appears in a variety of well positions across the study (Figure S4). This is achieved by creating different array layouts for each mouse in a given study. Once the first array has been designed, each subsequent array shifts the design of the first array by a random number of rows and columns (Figure S4A).

Concomitantly, we performed power analyses to determine how many biological and technical replicates would be needed to achieve high statistical power to detect effect sizes comparable to those seen in our initial vascular assembly data (Figure 2). Our analyses showed that we could screen up to 21 conditions, with two technical replicates for each condition in a given array, using as few as 8 mice (Figure S4B) and still detect effect sizes comparable to those seen within data in Figure 2. Based on these analyses, we created eight PHAST device maps, in which each array tests 21 experimental conditions with 2–3 technical replicates per array (Figure S4).

In addition, we next sought to investigate the potential likelihood of confounding variables such as crosstalk between wells of the array or systemic signaling. We reasoned cells known to be highly sensitive to biochemical and microenvironmental signals, such as monocytes from the peripheral blood, could be particularly useful for such studies. We thus deployed Tohoku

Hospital Pediatrics-1 (THP-1) cells, a human leukemia monocytic cell line that can be differentiated to macrophages.<sup>86</sup>

The THP-1 cells were first engineered to express firefly luciferase under the control of the signal transducer and activator of transcription 6 (STAT6) responsive elements, a marker for the pro-regenerative (M2) macrophage phenotype (THP-1-STAT6-fluc; Figure S5A). We then sought to validate that macrophages produced from these engineered cells are sensitive to molecules such as bacterial components like lipopolysaccharides (LPSs) and anti-inflammatory cytokines such as interleukin-4 (IL-4).<sup>87,88</sup> To do this, we differentiated the THP-1-STAT6-fluc cells to become macrophages in 2D culture (Figures S5B and S5C) and 3D culture in 5% GelMA (Figures S5B and S5D) within 96 well plates, wherein each condition was isolated from one another. We found that LPS suppressed STAT6 activity while IL-4 enhanced STAT6 activity (Figures S5C and S5D), in concordance with prior works in which LPS polarized macrophages to pro-inflammatory phenotype (M1) and IL-4 polarized macrophages to a pro-regenerative (M2) phenotype.<sup>87–91</sup>

We then used these reporter cells as a tool with which to report on potential crosstalk between wells. To do this, we first differentiated THP-1-STAT6-fluc cells with phorbol 12-myristate 13-acetate (PMA) for 48 h to produce macrophages. We then loaded LPS in 5% GelMA with these macrophages into the left-most two columns of the array, GelMA alone (N/A) with macrophages to the central three columns, and IL-4 in GelMA with macrophages to the right two columns (Figure S5E). We hypothesized that if the molecules diffused among the microwells, we would see all wells across the array exhibit similar levels of radiance. If LPS and IL-4 did not diffuse across the array in that enabled triggering of adjacent wells, the left-most two columns would exhibit low radiance, middle three columns exhibit medium radiance, and right two most columns exhibit high radiance.

After 2 days of *in vitro* culture, the right two columns containing IL-4 showed high STAT6-luciferase expression, whereas minimal expression was detected in the central and left columns (Figures S5F–S5H). These results indicate that the molecules in the wells did not substantively cross-contaminate between wells, at least in a manner that could then further trigger macrophage polarization to M1 or M2 phenotypes. Taken together, these studies suggest that the PHAST device design can overcome potential position effects and crosstalk to produce robust screening results.

### Scaling PHAST for combinatorial material and cellular screening *in vivo*

While most prior *in vivo* experiments have evaluated the influence of one variable at a time in implantable engineered tissues (e.g., material or cell formulation), microenvironmental ecosystems are composed of numerous interacting components, including extracellular matrices, cell populations such as stromal cells, and cell-secreted factors. We reasoned that the ability to screen many conditions *in vivo* would uniquely enable identification of the combinatorial effects of different classes of microenvironmental variables.

Thus, we next examined how combinatorial material-cellular interactions affect vascular assembly *in vivo*. Toward this end, stromal cells have been shown to enhance vascular self-assembly in engineered tissues upon their implantation in some set-

tings.<sup>38,67,92</sup> These findings, coupled with our observation of the importance of material microenvironment in vascular assembly (Figure 2), prompted our investigation of the combinatorial effect of different material formulations and inclusion of stromal cells (e.g., fibroblasts) on vascular assembly *in vivo*. We encapsulated endothelial cells in the presence or absence of human fibroblasts in various materials, such that individual wells were filled with microtissues consisting of 21 different material and cellular combinatorial formations (Figure 3A). These cells were encapsulated in an expanded portfolio of GelMA matrices, as well as a subset of natural hydrogels, including fibrin and collagen, two matrix components previously shown to support tissue vascularization<sup>92–94</sup> and cell transplantation<sup>95–98</sup> (Figure 3A). Each experimental condition had 2–3 technical replicates within each array, and arrays were laid out as denoted in Figure S4 to maximize power and minimize position bias.

Seeded PHAST arrays were implanted into mice for 2 weeks to test the impact of material and cell formulation on the formation and maintenance of self-assembled vascular networks lined with human endothelial cells *in vivo* (Figures 3 and S6). After explanting the PHAST arrays at 2 weeks, we immunostained and volumetrically imaged the arrays to visualize 3D human endothelial cell self-assembly (huCD31) and host RBCs (TER119). We then computationally reconstructed and parameterized networks across the arrays from each mouse (Figures 3B–3D and S6).

Our design had used a different array layout in each mouse (Figures 3 and S4) to protect against potential confounding by position effect, i.e., the possibility that the position of a given well (microtissue) within the array impacted outcome in PHAST vascular assembly studies. To assess the extent to which a position effect exists in these data, we performed statistical analyses to examine the “leftover” variation of huCD31 not explained by mouse effect or condition effect (Figure S7). We found no significant evidence of a position effect in the arrays (Figure S7B).

Importantly, consistent with our original device design goals and validation study (Figure S5), our statistical analyses also found no evidence of crosstalk between wells, indicating that if paracrine or diffusion interactions did occur, they did not significantly affect the experimental outcomes (Figure S7). Thus, careful design and implementation of array layout protected against the possibility of an undetected or misspecified position effect and well-to-well crosstalk, enabling us to reliably screen a high number of conditions using PHAST *in vivo*.

Our results demonstrated that in the absence of human fibroblasts, the lowest weight % GelMA materials best supported robust vascular self-assembly, in a manner dependent on GelMA dose (Figures 3D and 3E). Conversely and interestingly, when human fibroblasts were included in the microtissue, a larger range of material conditions supported robust vascular self-assembly, with lesser GelMA dose dependence (Figures 3D and 3E). Interestingly, inclusion of fibroblasts also expanded the range of materials that supported graft-host vascular inosculation and filling of graft networks with host blood (TER119<sup>+</sup>; Figure 3E). This corroborated other studies showing that the presence of stromal cells promoted vascular network formation and stabilization,<sup>38,39,67,99–101</sup> possibly by secreting pro-angiogenic growth factors,<sup>101,102</sup> transferring mitochondria to endothelial cells,<sup>101</sup> and/or remodeling extracellular matrix.<sup>103</sup>

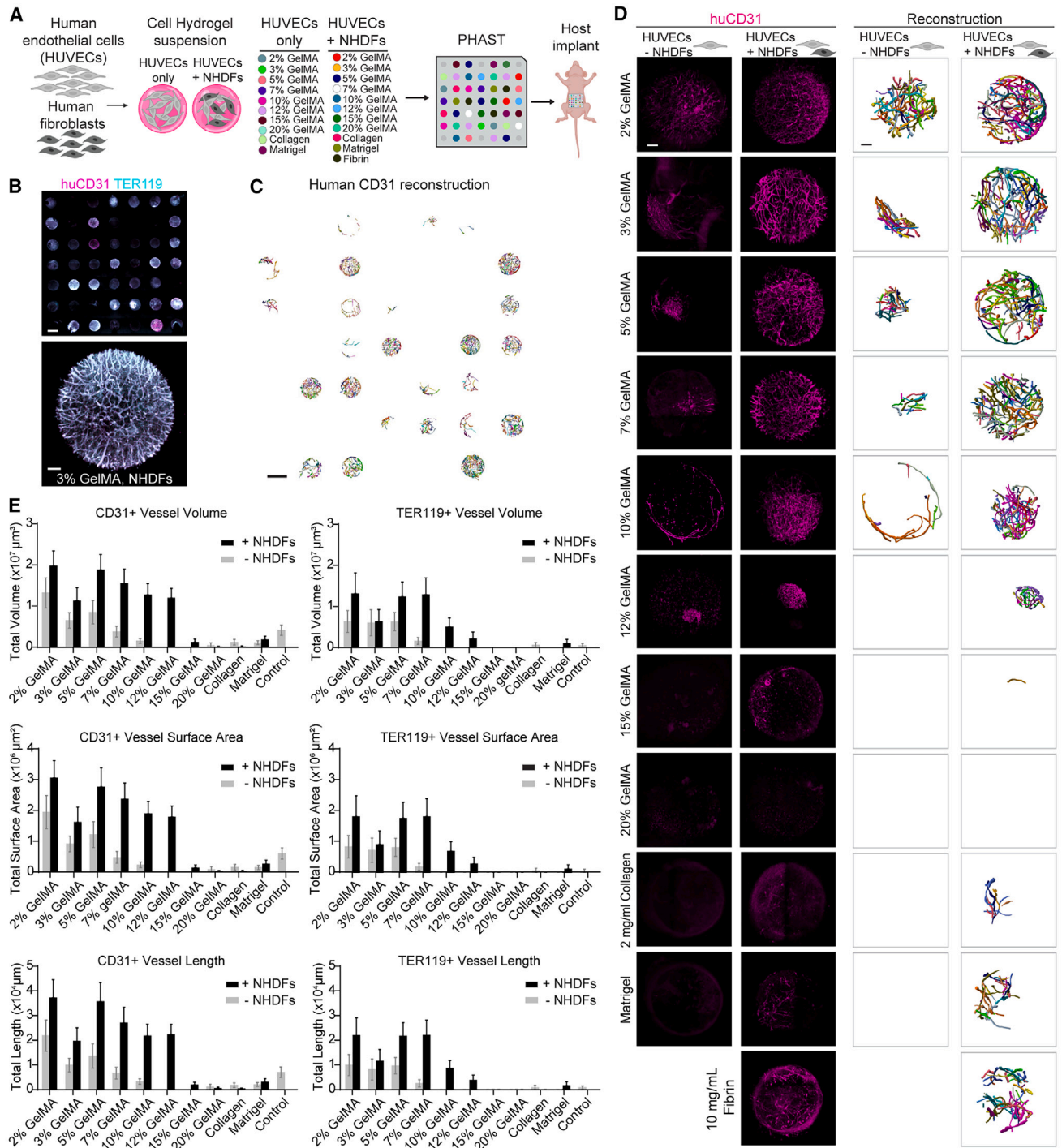


**Figure 3. PHAST for combinatorial screening of cellular and material microenvironments *in vivo***

(A) Experimental design screening 21 different material and cellular formulations, each with 2–3 technical replicates per array. Mice  $n = 8$ , each mouse receiving a different array layout.

(B) (Top) Representative PHAST array after 2 weeks *in vivo*, immunostained for huCD31 (magenta) and TER119 (cyan). Scale bar, 1 mm. (Bottom) Zoom-in of a well containing HUVECs with NHDFs in 3% GelMA. Scale bar, 100  $\mu\text{m}$ .

(C) Reconstructed 3D huCD31<sup>+</sup> self-assembled microvascular networks across an explanted PHAST array. Scale bar, 1 mm.

(D) (Left) Representative microtissues stained for huCD31 (magenta) within the 21 microenvironments screened. Scale bar, 100  $\mu\text{m}$ . (Right) Corresponding huCD31<sup>+</sup> self-assembled networks reconstructed in 3D. Scale bar, 100  $\mu\text{m}$ .

(E) (Left) Human CD31<sup>+</sup> and (Right) TER119<sup>+</sup> vascular network volume, surface area, and total length per microwell for each microenvironment screened. Data are represented as mean  $\pm$  SEM.

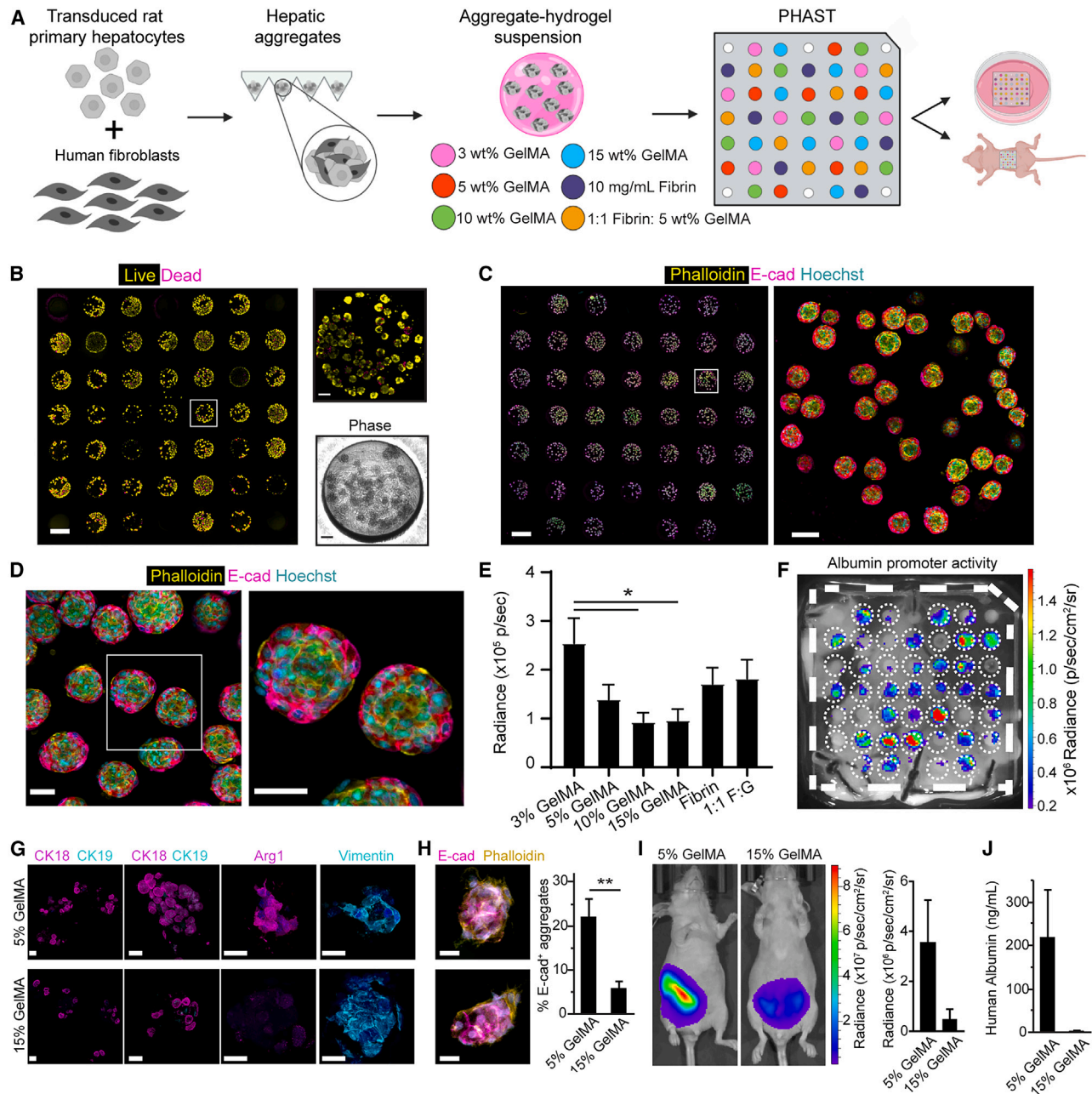


**Figure 4. PHAST screening engineered liver tissues across microenvironments**

(A) Experimental design. Hepatocytes were aggregated with fibroblasts to create hepatic aggregates, and aggregates were suspended in various material microenvironments (3%, 5%, 10%, 15% GelMA, 10 mg/mL fibrin, and 1:1 fibrin:5% GelMA) prior to filling in the PHAST arrays. Array map represents (F). Each material condition has 7 technical replicates per animal and 5 mouse hosts.

(B) (Left) A representative array filled with primary rat hepatocyte/NHDF aggregates and stained by live (calcein, yellow) and dead (ethidium homodimer, magenta) assay. Scale bar, 1 mm. (Right) Magnified (top) MIP and (bottom) phase contrast images of a single well. Scale bars, 100  $\mu$ m.

(C) (Left) An array with primary rat hepatocyte/NHDF aggregates immunostained for E-cadherin (E-cad, magenta, epithelial cell tight junctions), phalloidin (yellow, cell actin cytoskeleton), and Hoechst (cyan, cell nuclei). Scale bar, 1 mm. (Right) Magnified single microtissue in 5% GelMA. Scale bar, 100  $\mu$ m.

(D) (Left) Magnified view of 3D hepatic aggregates in 5% GelMA within a microwell. Scale bar, 50  $\mu$ m. (Right) 3D reconstruction of hepatic aggregates. Scale bar, 50  $\mu$ m.

(E and F) Albumin promoter-driven bioluminescent signal in various microenvironments after 8 days *in vivo*. (E) Quantitative analysis. \* $p < 0.05$  by one-way ANOVA followed by Tukey's post hoc test. (F) Representative *in vivo* imaging system (IVIS) image of a PHAST array.

(legend continued on next page)

We next leveraged the power of PHAST to rapidly assess the extent to which a variety of different stromal or supportive cell populations support vascular assembly and inosculation in different bioinks *in vivo*. We filled and implanted PHAST arrays containing microtissues with NHDFs, human mesenchymal stem cells (MSCs), or human dental pulp stem cells (DPSCs) in both 5% and 10% GelMA (Figure S8A). We found that for these formulations, the GelMA bioink wt % had a greater impact on the assembly of vascular networks that carry blood *in vivo* than did the type of support cell population (Figures S8B–S8D).

In summary, PHAST enabled combinatorial studies that incorporated both cellular and material variables. Furthermore, these studies revealed a phenomenon of stromal “rescue,” where the addition of fibroblasts to stiffer photoprintable bioinks commonly used for 3D bioprinting facilitates both vascular self-assembly and inosculation *in vivo*.

### Engineering liver tissues

Finally, we investigated the utility of PHAST to identify formulations of engineered tissues that could be used as therapeutic candidates for human disease and injury. We focused here on engineering liver tissue, which we and others are working to develop as a bridge therapy or alternative for whole organ transplantation.<sup>6</sup> Several groups have previously shown that delivering the liver’s main functional cells, called hepatocytes, directly into an injured liver is not effective for the most prevalent liver diseases, because the diseased (i.e., fibrotic or cirrhotic) host liver environment limits engraftment.<sup>32,104–108</sup> Thus, we and others are developing engineered liver tissue that can instead be implanted in an ectopic location, such as the perigonadal or mesenteric fat.<sup>10–12,62</sup> Here, we sought to identify materials that optimally support the survival and function of primary hepatocytes encased within such engineered tissues after implantation, which is an important step toward creating functional implantable tissues for treating liver disease.<sup>32</sup>

To do this, we first transduced rat primary hepatocytes with lentivirus in which luciferase is expressed under the albumin promoter, to later facilitate non-destructive detection of albumin promoter activity, a surrogate for hepatic function.<sup>106,109</sup> Transduced hepatocytes were then aggregated along with fibroblasts in microwells to create hepatic aggregates, which supports hepatic phenotype *in vitro* and survival *in vivo*.<sup>32,51,106</sup> Finally, we encapsulated hepatic aggregates within six different material formulations in distinct microtissue wells in the array (Figure 4A).

After *in vitro* encapsulation in the array, hepatic aggregates remained viable and expressed markers normally found on hepatocytes following photopolymerization within the PHAST array after 24 h of culture (Figures 4B and 4C). 3D reconstruction of the immunofluorescent signal from individual wells stained with E-cadherin and phalloidin demonstrated that hepatic aggregates retained a spherical morphology, with cells expressing E-cadherin-positive epithelial tight junctions generally localized to the perimeter of hepatic aggregates within array wells (Figures 4C and 4D).

After 8 days of implantation in athymic mice, we explanted the PHAST arrays and performed bioluminescence imaging to measure albumin promoter activity. We observed parallelized bioluminescent signal within individual wells across the array. We found that lowest wt % (softer) GelMA microenvironment supported the greatest albumin promoter activity in functioning hepatocytes after implantation, at a level of more than twice that of the least supportive materials (Figures 4E and 4F).

To validate and increase the translational impact of these results, we next tested whether cellular aggregates comprised of primary human hepatocytes and fibroblasts would similarly engraft within larger-scale (18 mm diameter, 1 mm thick) engineered liver tissues printed from 5% or 15% GelMA implanted into discrete mice (Figures 4G–4J). After 1 week of implantation, cells in explanted tissues expressed cytokeratin 18, a cytoskeletal protein expressed by hepatocytes, and arginase-1, a functional protein in hepatocytes that plays a key role in urea cycle (Figure 4G). Cells in explanted tissues were negative for cytokeratin 19, a cytoskeletal protein expressed by cholangiocytes, hepatoblasts, and bipotential cells, further suggesting the cells retained hepatocyte identity (Figure 4G). Some cells in explanted tissues expressed vimentin, a cytoskeletal protein found in cells of mesenchymal origin, consistent with our co-implantation of fibroblasts as supportive cells (Figure 4G). 3D immunostaining showed that many cells also expressed E-cadherin at the cell-cell junctions, consistent with hepatocytes (Figure 4H).

Importantly, grafted tissues exhibited albumin promoter activity (Figure 4I) and produced human albumin protein (Figure 4J), both of which are indicative of functional hepatocytes, with differential levels similar to those identified in PHAST. Thus, PHAST can be leveraged to identify tissue formulations that support the engraftment and survival of functional human engineered tissues *in vivo*.

### DISCUSSION

We report a platform for “plug and play” material- and cell-based screening *in vivo*, which we call PHAST. We used 3D printing technology<sup>51</sup> to print biocompatible hydrogel “well plates,” in which a single hydrogel slab contains 43 individually addressable wells, enabling creation and screening of engineered microtissues with different tissue components. PHAST enabled us to examine vascular self-assembly *in vivo*, by testing 21 different material/cellular formulations using only 8 animals. These studies revealed the combinatorial effects of different microenvironmental variables upon transplantation. This entire study, including all analyses, was completed in ~1–2 months. Using previous generation technologies, this study would have been logistically infeasible.

A major advantage of PHAST is its flexibility. Since PHAST arrays are built using 3D printing, the arrays could be rapidly tailored and fabricated to specific experimental questions, such as size and shape of each microwell. The PHAST array

(G–J) Larger scale discrete engineered liver tissues made from primary human hepatocytes/NHDF aggregates and 5% or 15% GelMA. One tissue per animal for 1 week.  $n = 7$ . Scale bars, 20  $\mu\text{m}$ . (G) Hepatic aggregates immunostained for cytokeratin 18 (CK18, magenta), cytokeratin 19 (CK19, cyan), arginase-1 (Arg1, magenta), and vimentin (cyan). (H) (Left) Hepatic aggregates 3D immunostained for E-cad (magenta) and phalloidin (yellow). (Right) Percentage of E-cad<sup>+</sup> aggregates. \*\* $p < 0.01$  by student’s  $t$  test. (I) (Left) Representative IVIS images and (right) quantitation of albumin promoter activity measured by bioluminescence in athymic mice. (J) Human albumin present in the mouse bloodstream in athymic mice. All data are represented as mean  $\pm$  SEM.

can also be scaled up for larger animal models, such as the array we built fit for a rat model. This flexibility enables future exploration of topics such as how tissue architecture and size impacts cellular behaviors after engraftment<sup>110,111</sup> or how findings might vary across animal models.<sup>112,113</sup>

Using PHAST, we found that numerous GelMA formulations supported at least some self-assembly of endothelial cells. Yet, only a subset of these materials also supported anastomosis of these self-assembled networks to host vessels, as well as their filling with mouse blood. While our studies corroborate work showing that softer matrices can better support cell behaviors such as self-organization compared with stiffer matrices,<sup>38,39,67,114–116</sup> the material-dependent mechanisms that drive such processes, such as stiffness of the material, ligand density, or porosity, need to be determined in future work. PHAST could help accelerate such mechanistic studies. Importantly, PHAST also further enabled us to identify microenvironments that are both “soft enough” to support vascular inosculation and “stiff enough” to be 3D printed. This is important, because balancing opposing biological and engineering design constraints has long stymied progress in fields such as biofabrication and bioprinting.<sup>117</sup>

We demonstrated potential translational relevance for PHAST platform by accelerating progress toward building engineering livers as a bridge or alternative to organ transplantation.<sup>32,106,118</sup> While our studies here focused on liver, PHAST could also be deployed to identify microenvironment formulations for other types of tissues. PHAST could also be deployed to accelerate personalized medicine, such as by probing how hepatocytes from different individual donors differentially metabolize drugs in different microenvironments *in vivo*.

Taken together, these studies demonstrate the potential power of PHAST for human tissue regeneration and repair applications. PHAST screening technology could also open paths toward a vast number of other medical applications, including not only tissue engineering but other areas, such as cancer bioengineering, personalized pharmacologic screening, and patient-specific therapeutic disease treatments.

### Limitations of the study

While we demonstrated that the PHAST array is a powerful tool for *in vivo* screening of engineered microenvironments, this technology in its current form cannot distinguish potential systematic responses, such as one well in an array eliciting a systemic response that then impacts all conditions. This is also limitation for other *in vivo* screening technologies, such as cellular barcoding technologies.<sup>119–123</sup> Nevertheless, this limitation means that scientists should be thoughtful about which applications are screened using PHAST. For example, we recommend using PHAST to screen materials that have been already shown to be biocompatible because a non-biocompatible formation could potentially impact the other wells.

A second potential limitation of our studies is that we chose to focus primarily on screening different formulations of GelMA, due to printability and adhesive moieties that support cell adhesion and self-organization. Notably, GelMA has potential drawbacks, such as lack of triple helix structure of native collagen,<sup>124</sup> limited mechanical robustness for load-bearing tissue such as bone, and potential for eliciting different cell behaviors compared with

other protein- or polysaccharide-based materials.<sup>35,114</sup> Importantly, such trade-offs are typical among most (and arguably all) biomaterials, whether synthetic, natural, or hybrid.<sup>35,114</sup> Nevertheless, future studies that further expand the portfolio of materials screened with PHAST would be useful.

A third potential limitation is that the PHAST studies here focused on mouse models, though we also demonstrated that PHAST arrays can be scaled up in size for rat studies. The largest arrays that could be printed using our current technology would be 62 × 38 mm (336 wells).<sup>51</sup> To produce arrays beyond these XY dimensions, such as for large animal studies, different printing hardware would be needed, arrays would need to be fabricated using other technologies, such as microtissue molding<sup>36,106</sup> or multiple smaller arrays would need to be implanted in a given animal.

Finally, in current form, PHAST arrays are designed for studies that use the intraperitoneal implant location in mice. Other implant locations and animal species have not yet been explored. Importantly, PHAST uses 3D printing technology, so rapid adjustments and iterations could presumably be made to array design and fabrication to produce arrays that custom fit other locations or species.

### RESOURCE AVAILABILITY

#### Lead contact

Additional information and requests for resources and reagents should be directed to and will be fulfilled by the lead contact, Kelly R. Stevens ([ksteve@uw.edu](mailto:ksteve@uw.edu)).

#### Materials availability

The PHAST array generated in this study will be made available on request, but we may require a payment and/or a completed materials transfer agreement if there is potential for commercial application.

#### Data and code availability

- All data reported in this paper have been deposited at Zenodo and are publicly available as of the date of publication at DOI: [10.5281/zenodo.15048024](https://doi.org/10.5281/zenodo.15048024).
- This paper does not report original code.
- Any additional information required to reanalyze the data reported in this paper is available from the [lead contact](#) upon request.

### ACKNOWLEDGMENTS

This research was supported by the NIH R01DK128551 (to K.R.S.), Wellcome Leap as part of the HOPE program (to K.R.S.), W.M. Keck Foundation (to K.R.S.), Allen Distinguished Investigator Award (to K.R.S.), a Paul G. Allen Frontiers Group advised grant of the Paul G. Allen Family Foundation (to K.R.S.), NIH Maximizing Investigators' Research Award (R35GM138036, to C.A.D.), NSF CAREER Award (DMR 1652141, to C.A.D.), NSF Graduate Research Fellowships (to C.E.O., S.P.S., N.E.G., and I.K.), a Ford Foundation Predoctoral Fellowship (to C.E.O.), NCATS Translational Research Training Program TL1 TR002318 (to C.L.F.), NIGMS Molecular Medicine training grant T32 GM095421 (to C.L.F.), and a Simons Investigator Award in Mathematical Modeling of Living Systems (to D.M.W.). Materials used in this research (PEGDA and lithium phenyl-2,4,6-trimethyl-benzoyl phosphinate [LAP]) were generously gifted by Dr. Jordan Miller at Rice University. We also thank Dr. Miller for feedback on this work.

### AUTHOR CONTRIBUTIONS

Conceptualization, C.E.O., F.Z., and K.R.S.; methodology, C.E.O., F.Z., and K.R.S.; investigation, C.E.O., F.Z., A.N., O.P., S.P.S., C.L.F., F.J., and J.M.;

formal analysis, C.E.O., F.Z., and A.N.; writing – original draft, C.E.O., F.Z., and K.R.S.; writing – review and editing, F.Z. and K.R.S.; visualization, C.E.O. and F.Z.; funding acquisition, K.R.S.; resources, S.H.S., I.K., N.E.G., and Z.J.; and supervision, K.R.S., D.M.W., E.C.W., and C.A.D.

#### DECLARATION OF INTERESTS

The authors declare no competing interests.

#### STAR★METHODS

Detailed methods are provided in the online version of this paper and include the following:

- **KEY RESOURCES TABLE**
- **EXPERIMENTAL MODEL AND STUDY PARTICIPANT DETAILS**
  - Animals
  - Primary cell cultures
  - Mouse and Rat Hepatocyte Isolation and Culture
- **METHOD DETAILS**
  - Design of PHAST array architectures
  - Polymer and photoinitiator synthesis
  - Material microenvironment synthesis and rheology characterization
  - Fabrication and Handling of PHAST arrays
  - Filling of PHAST arrays
  - Cell viability within PHAST array
  - Fabrication of discrete engineered tissues for result validation
  - In vivo implantation of PHAST arrays and discrete tissues
  - PHAST array harvesting, processing, and immunohistochemistry
  - PHAST array map design
  - Bioluminescent imaging
  - 2D tissue histology
  - Enzyme-Linked Immunosorbent Assay (ELISA)
- **QUANTIFICATION AND STATISTICAL ANALYSIS**
  - Linear models to account for mouse, condition, position, and crosstalk
  - Power analysis
  - Statistical analysis

#### SUPPLEMENTAL INFORMATION

Supplemental information can be found online at <https://doi.org/10.1016/j.stem.2025.03.002>.

Received: April 24, 2024

Revised: December 19, 2024

Accepted: March 4, 2025

Published: March 31, 2025

#### REFERENCES

1. Mitrousis, N., Fokina, A., and Shoichet, M.S. (2018). Biomaterials for cell transplantation. *Nat. Rev. Mater.* **3**, 441–456. <https://doi.org/10.1038/s41578-018-0057-0>.
2. Gaharwar, A.K., Singh, I., and Khademhosseini, A. (2020). Engineered biomaterials for in situ tissue regeneration. *Nat. Rev. Mater.* **5**, 686–705. <https://doi.org/10.1038/s41578-020-0209-x>.
3. Bianco, P., and Robey, P.G. (2001). Stem cells in tissue engineering. *Nature* **414**, 118–121.
4. Atala, A., Kurtis Kasper, F., and Mikos, A.G. (2012). Engineering complex tissues. *Sci. Transl. Med.* **4**, 160rv12. <https://doi.org/10.1038/35102181>.
5. Eugenis, I., Wu, D., Hu, C., Chiang, G., Huang, N.F., and Rando, T.A. (2022). Scalable macroporous hydrogels enhance stem cell treatment of volumetric muscle loss. *Biomaterials* **290**, 121818. <https://doi.org/10.1016/j.biomaterials.2022.121818>.
6. Li, S., Nih, L.R., Bachman, H., Fei, P., Li, Y., Nam, E., Dimatteo, R., Carmichael, S.T., Barker, T.H., Segura, T., Carmichael, S.T., Barker, T.H., and Segura, T. (2017). Hydrogels with precisely controlled integrin activation dictate vascular patterning and permeability. *Nat. Mater.* **16**, 953–961. <https://doi.org/10.1038/nmat4954>.
7. Richardson, T.P., Peters, M.C., Ennett, A.B., and Mooney, D.J. (2001). Polymeric system for dual growth factor delivery. *Nat. Biotechnol.* **19**, 1029–1034. <https://doi.org/10.1038/nbt1101-1029>.
8. Au, P., Tam, J., Fukumura, D., and Jain, R.K. (2008). Bone marrow-derived mesenchymal stem cells facilitate engineering of long-lasting functional vasculature. *Blood* **111**, 4551–4558. <https://doi.org/10.1182/blood-2007-10-118273>.
9. Kolesky, D.B., Homan, K.A., Skylar-Scott, M.A., and Lewis, J.A. (2016). Three-dimensional bioprinting of thick vascularized tissues. *Proc. Natl. Acad. Sci. USA* **113**, 3179–3184. <https://doi.org/10.1073/pnas.1521342113>.
10. Shen, Y.H., Shoichet, M.S., and Radisic, M. (2008). Vascular endothelial growth factor immobilized in collagen scaffold promotes penetration and proliferation of endothelial cells. *Acta Biomater.* **4**, 477–489. <https://doi.org/10.1016/j.actbio.2007.12.011>.
11. Ballios, B.G., Cooke, M.J., Donaldson, L., Coles, B.L.K., Morshead, C.M., van der Kooy, D., and Shoichet, M.S. (2015). A Hyaluronan-Based Injectable Hydrogel Improves the Survival and Integration of Stem Cell Progeny following Transplantation. *Stem Cell Rep.* **4**, 1031–1045. <https://doi.org/10.1016/j.stemcr.2015.04.008>.
12. Aguado, B.A., Mulyasmita, W., Su, J., Lampe, K.J., and Heilshorn, S.C. (2012). Improving viability of stem cells during syringe needle flow through the design of hydrogel cell carriers. *Tissue Eng. Part A* **18**, 806–815. <https://doi.org/10.1089/ten.TEA.2011.0391>.
13. Du, J., Zheng, L., Gao, P., Yang, H., Yang, W.J., Guo, F., Liang, R., Feng, M., Wang, Z., Zhang, Z., et al. (2022). A small-molecule cocktail promotes mammalian cardiomyocyte proliferation and heart regeneration. *Cell Stem Cell* **29**, 545–558.e13. <https://doi.org/10.1016/j.stem.2022.03.009>.
14. Wang, L.H., Marfil-Garza, B.A., Ernst, A.U., Pawlick, R.L., Pepper, A.R., Okada, K., Epel, B., Viswakarma, N., Kotecha, M., Flanders, J.A., et al. (2024). Inflammation-induced subcutaneous neovascularization for the long-term survival of encapsulated islets without immunosuppression. *Nat. Biomed. Eng.* **8**, 1266–1284. <https://doi.org/10.1038/s41551-023-01145-8>.
15. Engler, A.J., Sen, S., Sweeney, H.L., and Discher, D.E. (2006). Matrix elasticity directs stem cell lineage specification. *Cell* **126**, 677–689. <https://doi.org/10.1016/j.cell.2006.06.044>.
16. Park, S.H., Kwon, J.S., Lee, B.S., Park, J.H., Lee, B.K., Yun, J.H., Lee, B.Y., Kim, J.H., Min, B.H., Yoo, T.H., et al. (2017). BMP2-modified injectable hydrogel for osteogenic differentiation of human periodontal ligament stem cells. *Sci. Rep.* **7**, 6603. <https://doi.org/10.1038/s41598-017-06911-8>.
17. Moore, E.M., Maestas, D.R., Jr., Cherry, C.C., Garcia, J.A., Comeau, H.Y., Davenport Huyer, L., Kelly, S.H., Peña, A.N., Blosser, R.L., Rosson, G.D., et al. (2021). Biomaterials direct functional B cell response in a material-specific manner. *Sci. Adv.* **7**, eabj5830. <https://doi.org/10.1126/sciadv.abj5830>.
18. Jha, A., and Moore, E. (2022). Collagen-derived peptide, DGEA, inhibits pro-inflammatory macrophages in biofunctional hydrogels. *J. Mater. Res.* **37**, 77–87. <https://doi.org/10.1557/s43578-021-00423-y>.
19. Zhang, F., Gluck, J.M., Brown, A.C., Zaharoff, D.A., and King, M.W. (2023). Heparin affinity-based IL-4 delivery to modulate macrophage phenotype and endothelial cell activity in vitro. *ACS Appl. Mater. Interfaces* **15**, 27457–27470. <https://doi.org/10.1021/acsami.3c00489>.
20. Azarin, S.M., Yi, J., Gower, R.M., Aguado, B.A., Sullivan, M.E., Goodman, A.G., Jiang, E.J., Rao, S.S., Ren, Y., Tucker, S.L., et al. (2015). In vivo capture and label-free detection of early metastatic cells. *Nat. Commun.* **6**, 8094. <https://doi.org/10.1038/ncomms9094>.
21. Chen, T.T., Luque, A., Lee, S., Anderson, S.M., Segura, T., and Iruela-Arispe, M.L. (2010). Anchorage of VEGF to the extracellular matrix conveys differential signaling responses to endothelial cells. *J. Cell Biol.* **188**, 595–609. <https://doi.org/10.1083/jcb.200906044>.

22. Vegas, A.J., Veiseh, O., Gürtler, M., Millman, J.R., Pagliuca, F.W., Bader, A.R., Doloff, J.C., Li, J., Chen, M., Olejnik, K., et al. (2016). Long-term glycaemic control using polymer-encapsulated human stem cell-derived beta cells in immune-competent mice. *Nat. Med.* **22**, 306–311. <https://doi.org/10.1038/nm.4030>.
23. Fan, V.H., Tamama, K., Au, A., Littrell, R., Richardson, L.B., Wright, J.W., Wells, A., and Griffith, L.G. (2007). Tethered epidermal growth factor provides a survival advantage to mesenchymal stem cells. *Stem Cells* **25**, 1241–1251. <https://doi.org/10.1634/stemcells.2006-0320>.
24. Huang, K., Ozpinar, E.W., Su, T., Tang, J., Shen, D., Qiao, L., Hu, S., Li, Z., Liang, H., Mathews, K., et al. (2020). An off-the-shelf artificial cardiac patch improves cardiac repair after myocardial infarction in rats and pigs. *Sci. Transl. Med.* **12**, eaat9683. <https://doi.org/10.1126/scitranslmed.aat9683>.
25. Nakayama, K.H., Quarta, M., Paine, P., Alcazar, C., Karakikes, I., Garcia, V., Abilez, O.J., Calvo, N.S., Simmons, C.S., Rando, T.A., et al. (2019). Treatment of volumetric muscle loss in mice using nanofibrillar scaffolds enhances vascular organization and integration. *Commun. Biol.* **2**, 170. <https://doi.org/10.1038/s42003-019-0416-4>.
26. Zhang, F., and King, M.W. (2020). Biodegradable polymers as the pivotal player in the design of tissue engineering scaffolds. *Adv. Healthc. Mater.* **9**, e1901358. <https://doi.org/10.1002/adhm.201901358>.
27. Min, S., Cleveland, D., Ko, I.K., Kim, J.H., Yang, H.J., Atala, A., and Yoo, J.J. (2021). Accelerating neovascularization and kidney tissue formation with a 3D vascular scaffold capturing native vascular structure. *Acta Biomater.* **124**, 233–243. <https://doi.org/10.1016/j.actbio.2021.01.040>.
28. Bennett, J.I., Boit, M.O.K., Gregorio, N.E., Zhang, F., Kibler, R.D., Hoye, J.W., Prado, O., Rapp, P.B., Murry, C.E., Stevens, K.R., et al. (2024). Genetically Encoded XTEN-based Hydrogels with Tunable Viscoelasticity and Biodegradability for Injectable Cell Therapies. *Adv. Sci. (Weinh)* **11**, e2301708. <https://doi.org/10.1002/advs.202301708>.
29. Yang, L., Pijuan-Galito, S., Rho, H.S., Vasilevich, A.S., Eren, A.D., Ge, L., Habibović, P., Alexander, M.R., de Boer, J., Carlier, A., et al. (2021). High-throughput methods in the discovery and study of biomaterials and materiobiology. *Chem. Rev.* **121**, 4561–4677. <https://doi.org/10.1021/acs.chemrev.0c00752>.
30. Oliveira, M.B., Ribeiro, M.P., Miguel, S.P., Neto, A.I., Coutinho, P., Correia, I.J., and Mano, J.F. (2014). In vivo high-content evaluation of three-dimensional scaffolds biocompatibility. *Tissue Eng. Part C Methods* **20**, 851–864. <https://doi.org/10.1089/ten.TEC.2013.0738>.
31. Ng, S., March, S., Galstian, A., Gural, N., Stevens, K.R., Mota, M.M., and Bhatia, S.N. (2017). Towards a humanized mouse model of liver stage malaria using ectopic artificial livers. *Sci. Rep.* **7**, 45424. <https://doi.org/10.1038/srep45424>.
32. Stevens, K.R., Scull, M.A., Ramanan, V., Fortin, C.L., Chaturvedi, R.R., Knouse, K.A., Xiao, J.W., Fung, C., Mirabella, T., Chen, A.X., et al. (2017). In situ expansion of engineered human liver tissue in a mouse model of chronic liver disease. *Sci. Transl. Med.* **9**, eaah5505. <https://doi.org/10.1126/scitranslmed.aah5505>.
33. Murphy, W.L., Peters, M.C., Kohn, D.H., and Mooney, D.J. (2000). Sustained release of vascular endothelial growth factor from mineralized poly(lactide-co-glycolide) scaffolds for tissue engineering. *Biomaterials* **21**, 2521–2527. [https://doi.org/10.1016/s0142-9612\(00\)00120-4](https://doi.org/10.1016/s0142-9612(00)00120-4).
34. Freeman, I., and Cohen, S. (2009). The influence of the sequential delivery of angiogenic factors from affinity-binding alginate scaffolds on vascularization. *Biomaterials* **30**, 2122–2131. <https://doi.org/10.1016/j.biomaterials.2008.12.057>.
35. O'Connor, C., Brady, E., Zheng, Y., Moore, E., and Stevens, K.R. (2022). Engineering the multiscale complexity of vascular networks. *Nat. Rev. Mater.* **7**, 1–15. <https://doi.org/10.1038/s41578-022-00447-8>.
36. Baranski, J.D., Chaturvedi, R.R., Stevens, K.R., Eyckmans, J., Carvalho, B., Solorzano, R.D., Yang, M.T., Miller, J.S., Bhatia, S.N., Chen, C.S., Miller, J.S., Bhatia, S.N., and Chen, C.S. (2013). Geometric control of vascular networks to enhance engineered tissue integration and function. *Proc. Natl. Acad. Sci. USA* **110**, 7586–7591. <https://doi.org/10.1073/pnas.1217796110>.
37. Redd, M.A., Zeinstra, N., Qin, W., Wei, W., Martinson, A., Wang, Y., Wang, R.K., Murry, C.E., Zheng, Y., Murry, C.E., and Zheng, Y. (2019). Patterned human microvascular grafts enable rapid vascularization and increase perfusion in infarcted rat hearts. *Nat. Commun.* **10**, 584. <https://doi.org/10.1038/s41467-019-08388-7>.
38. Levenberg, S., Rouwkema, J., Macdonald, M., Garfein, E.S., Kohane, D.S., Darland, D.C., Marini, R., van Blitterswijk, C.A., Mulligan, R.C., D'Amore, P.A., et al. (2005). Engineering vascularized skeletal muscle tissue. *Nat. Biotechnol.* **23**, 879–884. <https://doi.org/10.1038/nbt1109>.
39. Kaully, T., Kaufman-Francis, K., Lesman, A., and Levenberg, S. (2009). Vascularization—the conduit to viable engineered tissues. *Tissue Eng. Part B Rev.* **15**, 159–169. <https://doi.org/10.1089/ten.teb.2008.0193>.
40. Vegas, A.J., Veiseh, O., Doloff, J.C., Ma, M., Tam, H.H., Bratlie, K., Li, J., Bader, A.R., Langan, E., Olejnik, K., et al. (2016). Combinatorial hydrogel library enables identification of materials that mitigate the foreign body response in primates. *Nat. Biotechnol.* **34**, 345–352. <https://doi.org/10.1038/nbt.3462>.
41. Mukherjee, S., Kim, B., Cheng, L.Y., Doerfert, M.D., Li, J., Hernandez, A., Liang, L., Jarvis, M.I., Rios, P.D., Ghani, S., et al. (2023). Screening hydrogels for antifibrotic properties by implanting cellularly barcoded alginates in mice and a non-human primate. *Nat. Biomed. Eng.* **7**, 867–886. <https://doi.org/10.1038/s41551-023-01016-2>.
42. Von Kortzfleisch, V.T., Karp, N.A., Palme, R., Kaiser, S., Sachser, N., and Richter, S.H. (2020). Improving reproducibility in animal research by splitting the study population into several 'mini-experiments'. *Sci. Rep.* **10**, 16579. <https://doi.org/10.1038/s41598-020-73503-4>.
43. Voelkl, B., Altman, N.S., Forsman, A., Forstmeier, W., Gurevitch, J., Jaric, I., Karp, N.A., Kas, M.J., Schielzeth, H., Van de Castelee, T., et al. (2020). Reproducibility of animal research in light of biological variation. *Nat. Rev. Neurosci.* **21**, 384–393. <https://doi.org/10.1038/s41583-020-0313-3>.
44. Higuera, G.A., Hendriks, J.A.A., van Dalum, J., Wu, L., Schotel, R., Moreira-Teixeira, L., van den Doel, M., Leijten, J.C.H., Riesle, J., Karperien, M., et al. (2013). In vivo screening of extracellular matrix components produced under multiple experimental conditions implanted in one animal. *Integr. Biol. (Camb)* **5**, 889–898. <https://doi.org/10.1039/c3ib40023a>.
45. Driehuis, E., Kretzschmar, K., and Clevers, H. (2020). Establishment of patient-derived cancer organoids for drug-screening applications. *Nat. Protoc.* **15**, 3380–3409. <https://doi.org/10.1038/s41596-020-0379-4>.
46. Eduati, F., Utharala, R., Madhavan, D., Neumann, U.P., Longrich, T., Cramer, T., Saez-Rodriguez, J., Merten, C.A., and Merten, C.A. (2018). A microfluidics platform for combinatorial drug screening on cancer biopsies. *Nat. Commun.* **9**, 2434. <https://doi.org/10.1038/s41467-018-04919-w>.
47. Mathews Griner, L.A., Guha, R., Shinn, P., Young, R.M., Keller, J.M., Liu, D., Goldlust, I.S., Yasgar, A., McKnight, C., Boxer, M.B., et al. (2014). High-throughput combinatorial screening identifies drugs that cooperate with ibrutinib to kill activated B-cell-like diffuse large B-cell lymphoma cells. *Proc. Natl. Acad. Sci. USA* **111**, 2349–2354. <https://doi.org/10.1073/pnas.1311846111>.
48. Huang, L., Holtzinger, A., Jagan, I., BeGora, M., Lohse, I., Ngai, N., Nostro, C., Wang, R., Muthuswamy, L.B., Crawford, H.C., et al. (2015). Ductal pancreatic cancer modeling and drug screening using human pluripotent stem cell- and patient-derived tumor organoids. *Nat. Med.* **21**, 1364–1371. <https://doi.org/10.1038/nm.3973>.
49. Flaim, C.J., Chien, S., and Bhatia, S.N. (2005). An extracellular matrix microarray for probing cellular differentiation. *Nat. Methods* **2**, 119–125. <https://doi.org/10.1038/nmeth736>.
50. Beachley, V.Z., Wolf, M.T., Sadtler, K., Manda, S.S., Jacobs, H., Blatchley, M.R., Bader, J.S., Pandey, A., Pardoll, D., Elisseeff, J.H., Pandey, A., Pardoll, D., and Elisseeff, J.H. (2015). Tissue matrix arrays for high-throughput screening and systems analysis of cell function. *Nat. Methods* **12**, 1197–1204. <https://doi.org/10.1038/nmeth.3619>.
51. Grigoryan, B., Paulsen, S.J., Corbett, D.C., Sazer, D.W., Fortin, C.L., Zaita, A.J., Greenfield, P.T., Calafat, N.J., Gounley, J.P., Ta, A.H., et al. (2019). Multivascular networks and functional intravascular topologies

- within biocompatible hydrogels. *Science* 364, 458–464. <https://doi.org/10.1126/science.aav9750>.
52. Richbourg, N.R., Wancura, M., Gilchrist, A.E., Toubbeh, S., Harley, B.A.C., Cosgriff-Hernandez, E., and Peppas, N.A. (2021). Precise control of synthetic hydrogel network structure via linear, independent synthesis-swelling relationships. *Sci. Adv.* 7, eabe3245. <https://doi.org/10.1126/sciadv.abe3245>.
  53. Chen, Z., Hu, X., Lin, Z., Mao, H., Qiu, Z., Xiang, K., Ke, T., Li, L., Lu, L., Xiao, L., Li, L., Lu, L., and Xiao, L. (2023). Layered GelMA/PEGDA hydrogel microneedle patch as an intradermal delivery system for hypertrophic scar treatment. *ACS Appl. Mater. Interfaces* 15, 43309–43320. <https://doi.org/10.1021/acsmami.3c06800>.
  54. Wang, Y., Ma, M., Wang, J., Zhang, W., Lu, W., Gao, Y., Zhang, B., Guo, Y., and Guo, Y. (2018). Development of a Photo-Crosslinking, Biodegradable GelMA/PEGDA Hydrogel for Guided Bone Regeneration Materials. *Materials (Basel)* 11, 1345. <https://doi.org/10.3390/ma11081345>.
  55. Yue, K., Trujillo-de Santiago, G., Alvarez, M.M., Tamayol, A., Annabi, N., and Khademhosseini, A. (2015). Synthesis, properties, and biomedical applications of gelatin methacryloyl (GelMA) hydrogels. *Biomaterials* 73, 254–271. <https://doi.org/10.1016/j.biomaterials.2015.08.045>.
  56. Rizwan, M., Chan, S.W., Comeau, P.A., Willett, T.L., and Yim, E.K.F. (2020). Effect of sterilization treatment on mechanical properties, biodegradation, bioactivity and printability of GelMA hydrogels. *Biomed. Mater.* 15, 065017. <https://doi.org/10.1088/1748-605X/aba40c>.
  57. Yuan, M., Liu, K., Jiang, T., Li, S., Chen, J., Wu, Z., Li, W., Tan, R., Wei, W., Yang, X., et al. (2022). GelMA/PEGDA microneedles patch loaded with HUVECs-derived exosomes and tazarotene promote diabetic wound healing. *J. Nanobiotechnology* 20, 147. <https://doi.org/10.1186/s12951-022-01354-4>.
  58. De Jesus Morales, K.J., Santosa, U., Brazhkina, O., Rajurkar, P., Jo, H., and Davis, M.E. (2024). A Biomimetic Leaflet Scaffold for Aortic Valve Remodeling. *Adv. Healthc. Mater.* 13, e2303972. <https://doi.org/10.1002/adhm.202303972>.
  59. Gama Sosa, M.A., De Gasperi, R., Perez Garcia, G.S., Perez, G.M., Searcy, C., Vargas, D., Spencer, A., Janssen, P.L., Tschiffely, A.E., McCarron, R.M., et al. (2019). Low-level blast exposure disrupts gliovascular and neurovascular connections and induces a chronic vascular pathology in rat brain. *Acta Neuropathol. Commun.* 7, 6. <https://doi.org/10.1186/s40478-018-0647-5>.
  60. Mansour, A.A., Gonçalves, J.T., Bloyd, C.W., Li, H., Fernandes, S., Quang, D., Johnston, S., Parylak, S.L., Jin, X., Gage, F.H., Parylak, S.L., Jin, X., and Gage, F.H. (2018). An in vivo model of functional and vascularized human brain organoids. *Nat. Biotechnol.* 36, 432–441. <https://doi.org/10.1038/nbt.4127>.
  61. Zhang, F., and King, M.W. (2022). Immunomodulation strategies for the successful regeneration of a tissue-engineered vascular graft. *Adv. Healthc. Mater.* 11, e2200045. <https://doi.org/10.1002/adhm.202200045>.
  62. Takebe, T., Sekine, K., Enomura, M., Koike, H., Kimura, M., Ogaeri, T., Zhang, R.R., Ueno, Y., Zheng, Y.W., Koike, N., et al. (2013). Vascularized and functional human liver from an iPSC-derived organ bud transplant. *Nature* 499, 481–484. <https://doi.org/10.1038/nature12271>.
  63. Lee, A.R.H.A., Hudson, A.R., Shiwarski, D.J., Tashman, J.W., Hinton, T.J., Yerneni, S., Bliley, J.M., Campbell, P.G., and Feinberg, A.W. (2019). 3D bioprinting of collagen to rebuild components of the human heart. *Science* 365, 482–487. <https://doi.org/10.1126/science.aav9051>.
  64. Koike, N., Fukumura, D., Gralla, O., Au, P., Schechner, J.S., and Jain, R.K. (2004). Tissue engineering: Creation of long-lasting blood vessels. *Nature* 428, 138–139. <https://doi.org/10.1038/428138a>.
  65. Stratman, A.N., Malotte, K.M., Mahan, R.D., Davis, M.J., and Davis, G.E. (2009). Pericyte recruitment during vasculogenic tube assembly stimulates endothelial basement membrane matrix formation. *Blood* 114, 5091–5101. <https://doi.org/10.1182/blood-2009-05-222364>.
  66. Song, H.G., Lammers, A., Sundaram, S., Rubio, L., Chen, A.X., Li, L., Eyckmans, J., Bhatia, S.N., and Chen, C.S. (2020). Transient Support from Fibroblasts is Sufficient to Drive Functional Vascularization in Engineered Tissues. *Adv. Funct. Mater.* 30, 2003777. <https://doi.org/10.1002/adfm.202003777>.
  67. Stevens, K.R., Kreutziger, K.L., Dupras, S.K., Korte, F.S., Regnier, M., Muskheli, V., Nourse, M.B., Bendixen, K., Reinecke, H., Murry, C.E., Bendixen, K., Reinecke, H., and Murry, C.E. (2009). Physiological function and transplantation of scaffold-free and vascularized human cardiac muscle tissue. *Proc. Natl. Acad. Sci. USA* 106, 16568–16573. <https://doi.org/10.1073/pnas.0908381106>.
  68. Kreutziger, K.L., Muskheli, V., Johnson, P., Braun, K., Wight, T.N., and Murry, C.E. (2011). Developing vasculature and stroma in engineered human myocardium. *Tissue Eng. Part A* 17, 1219–1228. <https://doi.org/10.1089/ten.TEA.2010.0557>.
  69. Benton, J.A., DeForest, C.A., Vivekanandan, V., and Anseth, K.S. (2009). Photocrosslinking of Gelatin Macromers to Synthesize Porous Hydrogels That Promote Valvular Interstitial Cell Function. *Tissue Eng. Part A* 15, 3221–3230. <https://doi.org/10.1089/ten.TEA.2008.0545>.
  70. Zhu, M., Wang, Y., Ferracci, G., Zheng, J., Cho, N.J., and Lee, B.H. (2019). Gelatin methacryloyl and its hydrogels with an exceptional degree of controllability and batch-to-batch consistency. *Sci. Rep.* 9, 6863. <https://doi.org/10.1038/s41598-019-42186-x>.
  71. Nichol, J.W., Koshy, S.T., Bae, H., Hwang, C.M., Yamanlar, S., and Khademhosseini, A. (2010). Cell-laden microengineered gelatin methacrylate hydrogels. *Biomaterials* 31, 5536–5544. <https://doi.org/10.1016/j.biomaterials.2010.03.064>.
  72. Shin, S.R., Aghaei-Ghareh-Bolagh, B., Dang, T.T., Topkaya, S.N., Gao, X., Yang, S.Y., Jung, S.M., Oh, J.H., Dokmeci, M.R., Tang, X.S., et al. (2013). Cell-laden microengineered and mechanically tunable hybrid hydrogels of gelatin and graphene oxide. *Adv. Mater.* 25, 6385–6391. <https://doi.org/10.1002/adma.201301082>.
  73. Butenko, S., Nagalla, R.R., Guerrero-Juarez, C.F., Palomba, F., David, L.M., Nguyen, R.Q., Gay, D., Almet, A.A., Digham, M.A., Nie, Q., et al. (2024). Hydrogel crosslinking modulates macrophages, fibroblasts, and their communication, during wound healing. *Nat. Commun.* 15, 6820. <https://doi.org/10.1038/s41467-024-50072-y>.
  74. Shirahama, H., Lee, B.H., Tan, L.P., and Cho, N.-J. (2016). Precise Tuning of Facile One-Pot Gelatin Methacryloyl (GelMA) Synthesis. *Nat. Publ. Gr.* <https://doi.org/10.1038/srep31036>.
  75. Klak, M., Gomółka, M., Dobrzański, T., Tymicki, G., Cywoniuk, P., Kowalska, P., Kosowska, K., Bryniarski, T., Berman, A., Dobrzyń, A., et al. (2020). Irradiation with 365 nm and 405 nm wavelength shows differences in DNA damage of swine pancreatic islets. *PLoS One* 15, e0235052. <https://doi.org/10.1371/journal.pone.0235052>.
  76. Lawrence, K.P., Douki, T., Sarkany, R.P.E., Acker, S., Herzog, B., and Young, A.R. (2018). The UV/Visible Radiation Boundary Region (385–405 nm) Damages Skin Cells and Induces “dark” Cyclobutane Pyrimidine Dimers in Human Skin in vivo. *Sci. Rep.* 8, 12722. <https://doi.org/10.1038/s41598-018-30738-6>.
  77. Li, W., Germain, R.N., and Gerner, M.Y. (2017). Multiplex, quantitative cellular analysis in large tissue volumes with clearing-enhanced 3D microscopy (Ce3D). *Proc. Natl. Acad. Sci. USA* 114, E7321–E7330. <https://doi.org/10.1073/pnas.1708981114>.
  78. Nelson, C.M., VanDuijn, M.M., Inman, J.L., Fletcher, D.A., and Bissell, M.J. (2006). Tissue geometry determines sites of mammary branching morphogenesis in organotypic cultures. *Science* 314, 298–300. <https://doi.org/10.1126/science.1131000>.
  79. Chen, C.S., Mrksich, M., Huang, S., Whitesides, G.M., and Ingber, D.E. (1997). Geometric control of cell life and death. *Science* 276, 1425–1428. <https://doi.org/10.1126/science.276.5317.1425>.
  80. Gjorevski, N., Nikolaev, M., Brown, T.E., Mitrofanova, O., Brandenberg, N., DelRio, F.W., Yavitt, F.M., Liberali, P., Anseth, K.S., and Lutolf, M.P. (2022). Tissue geometry drives deterministic organoid patterning. *Science* 375, eaaw9021. <https://doi.org/10.1126/science.aaw9021>.
  81. Li, J., Moeinzadeh, S., Kim, C., Pan, C.C., Weale, G., Kim, S., Abrams, G., James, A.W., Choo, H., Chan, C., et al. (2023). Development and systematic characterization of GelMA/alginate/PEGDMA/xanthan gum hydrogel

- bioink system for extrusion bioprinting. *Biomaterials* 293, 121969. <https://doi.org/10.1016/j.biomaterials.2022.121969>.
82. de Barros, N.R., Gomez, A., Ermis, M., Falcone, N., Haghniaz, R., Young, P., Gao, Y., Aquino, A.F., Li, S., Niu, S., et al. (2023). Gelatin methacryloyl and laponite bioink for 3D bioprinted organotypic tumor modeling. *Biofabrication* 15, 045005. <https://doi.org/10.1088/1758-5090/ace0db>.
  83. Zhang, F., Tao, H., Gluck, J.M., Wang, L., Daneshmand, M.A., and King, M.W. (2023). A textile-reinforced composite vascular graft that modulates macrophage polarization and enhances endothelial cell migration, adhesion and proliferation in vitro. *Soft Matter* 19, 1624–1641. <https://doi.org/10.1039/d2sm01190e>.
  84. Jin, R., Cui, Y., Chen, H., Zhang, Z., Weng, T., Xia, S., Yu, M., Zhang, W., Shao, J., Yang, M., et al. (2021). Three-dimensional bioprinting of a full-thickness functional skin model using acellular dermal matrix and gelatin methacrylamide bioink. *Acta Biomater.* 131, 248–261. <https://doi.org/10.1016/j.actbio.2021.07.012>.
  85. Visser, J., Melchels, F.P.W., Jeon, J.E., Van Bussel, E.M., Kimpton, L.S., Byrne, H.M., Dhert, W.J.A., Dalton, P.D., Huttmacher, D.W., and Malda, J. (2015). Reinforcement of hydrogels using three-dimensionally printed microfibrils. *Nat. Commun.* 6, 6933. <https://doi.org/10.1038/ncomms7933>.
  86. Tsuchiya, S., Yamabe, M., Yamaguchi, Y., Kobayashi, Y., Konno, T., and Tada, K. (1980). Establishment and characterization of a human acute monocytic leukemia cell line (THP-1). *Int. J. Cancer* 26, 171–176.
  87. Locati, M., Curtale, G., and Mantovani, A. (2020). Diversity, mechanisms, and significance of macrophage plasticity. *Annu. Rev. Pathol.* 15, 123–147. <https://doi.org/10.1146/annurev-pathmechdis-012418-012718>.
  88. Graney, P.L., Ben-Shaul, S., Landau, S., Bajpai, A., Singh, B., Eager, J., Cohen, A., Levenberg, S., and Spiller, K.L. (2020). Macrophages of diverse phenotypes drive vascularization of engineered tissues. *Sci. Adv.* 6, eaay6391. <https://doi.org/10.1126/sciadv.aay6391>.
  89. Spiller, K.L., Anfang, R.R., Spiller, K.J., Ng, J., Nakazawa, K.R., Daulton, J.W., and Vunjak-Novakovic, G. (2014). The role of macrophage phenotype in vascularization of tissue engineering scaffolds. *Biomaterials* 35, 4477–4488. <https://doi.org/10.1016/j.biomaterials.2014.02.012>.
  90. Yu, T., Gan, S., Zhu, Q., Dai, D., Li, N., Wang, H., Chen, X., Hou, D., Wang, Y., Pan, Q., et al. (2019). Modulation of M2 macrophage polarization by the crosstalk between Stat6 and Trim24. *Nat. Commun.* 10, 4353. <https://doi.org/10.1038/s41467-019-12384-2>.
  91. Zheng, S., Chiang, Y.H., Aldarondo, D., Fox, Z.R., Akpa, B.S., and Wayne, E. Capturing the Dynamics of STAT6 Macrophage Polarization Using Bioluminescence Temporal Spectrometry. Available at SSRN 4682259. <https://doi.org/10.2139/ssrn.4682259>.
  92. Cheng, G., Liao, S., Kit Wong, H., Lacorre, D.A., Di Tomaso, E., Au, P., Fukumura, D., Jain, R.K., and Munn, L.L. (2011). Engineered blood vessel networks connect to host vasculature via wrapping-and-tapping anastomosis. *Blood* 118, 4740–4749. <https://doi.org/10.1182/blood-2011-02-338426>.
  93. Shaikh, F.M., Callanan, A., Kavanagh, E.G., Burke, P.E., Grace, P.A., and McGloughlin, T.M. (2008). Fibrin: a natural biodegradable scaffold in vascular tissue engineering. *Cells Tissues Organs* 188, 333–346. <https://doi.org/10.1159/000139772>.
  94. Suuronen, E.J., Veinot, J.P., Wong, S., Kapila, V., Price, J., Griffith, M., Mesana, T.G., and Ruel, M. (2006). Tissue-engineered injectable collagen-based matrices for improved cell delivery and vascularization of ischemic tissue using CD133+ progenitors expanded from the peripheral blood. *Circulation* 114, I138–I144. <https://doi.org/10.1161/CIRCULATIONAHA.105.001081>.
  95. Mimura, T., Yamagami, S., Yokoo, S., Usui, T., Tanaka, K., Hattori, S., Irie, S., Miyata, K., Araie, M., Amano, S., Miyata, K., Araie, M., and Amano, S. (2004). Cultured Human Corneal Endothelial Cell Transplantation with a Collagen Sheet in a Rabbit Model. *Invest. Ophthalmol. Vis. Sci.* 45, 2992–2997. <https://doi.org/10.1167/iovs.03-1174>.
  96. Zhang, Y., Thorn, S., DaSilva, J.N., Lamoureux, M., DeKemp, R.A., Beanlands, R.S., Ruel, M., and Suuronen, E.J. (2008). Collagen-based matrices improve the delivery of transplanted circulating progenitor cells: development and demonstration by ex vivo radionuclide cell labeling and in vivo tracking with positron-emission tomography. *Circ. Cardiovasc. Imaging* 7, 197–204. <https://doi.org/10.1161/CIRCIMAGING.108.781120>.
  97. Christman, K.L., Vardanian, A.J., Fang, Q., Sievers, R.E., Fok, H.H., and Lee, R.J. (2004). Injectable fibrin scaffold improves cell transplant survival, reduces infarct expansion, and induces neovascularization formation in ischemic myocardium. *J. Am. Coll. Cardiol.* 44, 654–660. <https://doi.org/10.1016/j.jacc.2004.04.040>.
  98. Bensaid, W., Triffitt, J.T., Blanchat, C., Oudina, K., Sedel, L., and Petite, H. (2003). A biodegradable fibrin scaffold for mesenchymal stem cell transplantation. *Biomaterials* 24, 2497–2502. [https://doi.org/10.1016/s0142-9612\(02\)00618-x](https://doi.org/10.1016/s0142-9612(02)00618-x).
  99. Griffith, C.K., Miller, C., Sainson, R.C.A., Calvert, J.W., Jeon, N.L., Hughes, C.C.W., and George, S.C. (2005). Diffusion limits of an in vitro thick prevascularized tissue. *Tissue Eng.* 11, 257–266. <https://doi.org/10.1089/ten.2005.11.257>.
  100. Chen, X., Aledia, A.S., Popson, S.A., Him, L., Hughes, C.C.W., and George, S.C. (2010). Rapid anastomosis of endothelial progenitor cell-derived vessels with host vasculature is promoted by a high density of cotransplanted fibroblasts. *Tissue Eng. Part A* 16, 585–594. <https://doi.org/10.1089/ten.TEA.2009.0491>.
  101. Lin, R.Z., Im, G.B., Luo, A.C., Zhu, Y., Hong, X., Neumeyer, J., Tang, H.W., Perrimon, N., and Melero-Martin, J.M. (2024). Mitochondrial transfer mediates endothelial cell engraftment through mitophagy. *Nature* 629, 660–668. <https://doi.org/10.1038/s41586-024-07340-0>.
  102. Liu, H., Chen, B., and Lilly, B. (2008). Fibroblasts potentiate blood vessel formation partially through secreted factor TIMP-1. *Angiogenesis* 11, 223–234. <https://doi.org/10.1007/s10456-008-9102-8>.
  103. Berthod, F., Germain, L., Tremblay, N., and Auger, F.A. (2006). Extracellular matrix deposition by fibroblasts is necessary to promote capillary-like tube formation in vitro. *J. Cell. Physiol.* 207, 491–498.
  104. Corbett, D.C., Fabyan, W.B., Grigoryan, B., O'Connor, C.E., Johansson, F., Batalov, I., Regier, M.C., DeForest, C.A., Miller, J.S., and Stevens, K.R. (2020). Thermofluidic heat exchangers for actuation of transcription in artificial tissues. *Sci. Adv.* 6, eaab9062. <https://doi.org/10.1126/sciadv.aab9062>.
  105. Hickey, R.D., and Naugler, W.E. (2018). Ectopic expansion of engineered human liver tissue seeds using mature cell populations. *Hepatology* 67, 2465–2467. <https://doi.org/10.1002/hep.29718>.
  106. Stevens, K.R., Ungrin, M.D., Schwartz, R.E., Ng, S., Carvalho, B., Christine, K.S., Chaturvedi, R.R., Li, C.Y., Zandstra, P.W., Chen, C.S., et al. (2013). InVERT molding for scalable control of tissue microarchitecture. *Nat. Commun.* 4, 1847. <https://doi.org/10.1038/ncomms2853>.
  107. Hoppo, T., Komori, J., Manohar, R., Stolz, D.B., and Lagasse, E. (2011). Rescue of lethal hepatic failure by hepated lymph nodes in mice. *Gastroenterology* 140, 656–666.e2. <https://doi.org/10.1053/j.gastro.2010.11.006>.
  108. Komori, J., Boone, L., DeWard, A., Hoppo, T., and Lagasse, E. (2012). The mouse lymph node as an ectopic transplantation site for multiple tissues. *Nat. Biotechnol.* 30, 976–983. <https://doi.org/10.1038/nbt.2379>.
  109. Andrus, L., Marukian, S., Jones, C.T., Catanese, M.T., Sheahan, T.P., Schoggins, J.W., Barry, W.T., Dustin, L.B., Trehan, K., Ploss, A., et al. (2011). Expression of paramyxovirus V proteins promotes replication and spread of hepatitis C virus in cultures of primary human fetal liver cells. *Hepatology* 54, 1901–1912. <https://doi.org/10.1002/hep.24557>.
  110. Nelson, C.M., Jean, R.P., Tan, J.L., Liu, W.F., Sniadecki, N.J., Spector, A.A., and Chen, C.S. (2005). Emergent patterns of growth controlled by multicellular form and mechanics. *Proc. Natl. Acad. Sci. USA* 102, 11594–11599. <https://doi.org/10.1073/pnas.0502575102>.
  111. Yang, Q., Xue, S.L., Chan, C.J., Rempfler, M., Vischi, D., Maurer-Gutierrez, F., Hiriagi, T., Hannezo, E., and Liberali, P. (2021). Cell fate coordinates mechano-osmotic forces in intestinal crypt formation. *Nat. Cell Biol.* 23, 733–744. <https://doi.org/10.1038/s41556-021-00700-2>.

112. Brady, E.L., Kirby, M.A., Olszewski, E., Grosjean, P., Johansson, F., Davis, J., Wang, R.K., and Stevens, K.R. (2020). Guided vascularization in the rat heart leads to transient vessel patterning. *APL Bioeng.* 4, 016105. <https://doi.org/10.1063/1.5122804>.
113. Brady, E.L., Prado, O., Johansson, F., Mitchell, S.N., Martinson, A.M., Karbassi, E., Reinecke, H., Murry, C.E., Davis, J., and Stevens, K.R. (2023). Engineered tissue vascularization and engraftment depends on host model. *Sci. Rep.* 13, 1973. <https://doi.org/10.1038/s41598-022-23895-2>.
114. Atcha, H., Choi, Y.S., Chaudhuri, O., and Engler, A.J. (2023). Getting physical: material mechanics is an intrinsic cell cue. *Cell Stem Cell* 30, 750–765. <https://doi.org/10.1016/j.stem.2023.05.003>.
115. Wei, Z., Schnellmann, R., Pruitt, H.C., and Gerecht, S. (2020). Hydrogel network dynamics regulate vascular morphogenesis. *Cell Stem Cell* 27, 798–812.e6. <https://doi.org/10.1016/j.stem.2020.08.005>.
116. Huebsch, N., Arany, P.R., Mao, A.S., Shvartsman, D., Ali, O.A., Bencherif, S.A., Rivera-Feliciano, J., and Mooney, D.J. (2010). Harnessing traction-mediated manipulation of the cell/matrix interface to control stem-cell fate. *Nat. Mater.* 9, 518–526. <https://doi.org/10.1038/nmat2732>.
117. Corbett, D.C., Olszewski, E., and Stevens, K.R. (2019). A FRESH take on resolution in 3D bioprinting. *Trends Biotechnol.* 37, 1153–1155. <https://doi.org/10.1016/j.tibtech.2019.09.003>.
118. Kim, D.H., Kim, M.J., Kwak, S.Y., Jeong, J., Choi, D., Choi, S.W., Ryu, J., and Kang, K.S. (2023). Bioengineered liver crosslinked with nano-graphene oxide enables efficient liver regeneration via MMP suppression and immunomodulation. *Nat. Commun.* 14, 801. <https://doi.org/10.1038/s41467-023-35941-2>.
119. Michels, B.E., Mosa, M.H., Streibl, B.I., Zhan, T., Menche, C., Abou-El-Ardat, K., Darvishi, T., Czlonka, E., Wagner, S., Winter, J., et al. (2020). Pooled in vitro and in vivo CRISPR-Cas9 screening identifies tumor suppressors in human colon organoids. *Cell Stem Cell* 26, 782–792.e7. <https://doi.org/10.1016/j.stem.2020.04.003>.
120. Parvez, S., Herdman, C., Beerens, M., Chakraborti, K., Harmer, Z.P., Yeh, J.J., MacRae, C.A., Yost, H.J., and Peterson, R.T. (2021). MIC-Drop: A platform for large-scale in vivo CRISPR screens. *Science* 373, 1146–1151. <https://doi.org/10.1126/science.abi8870>.
121. Roth, T.L., Li, P.J., Blaeschke, F., Nies, J.F., Apathy, R., Mowery, C., Yu, R., Nguyen, M.L.T., Lee, Y., Truong, A., et al. (2020). Pooled knockin targeting for genome engineering of cellular immunotherapies. *Cell* 181, 728–744.e21. <https://doi.org/10.1016/j.cell.2020.03.039>.
122. Bortolotti, F., Ruozi, G., Falcione, A., Doimo, S., Dal Ferro, M., Lesizza, P., Zentilin, L., Banks, L., Zacchigna, S., and Giacca, M. (2017). In vivo functional selection identifies cardiotrophin-1 as a cardiac engraftment factor for mesenchymal stromal cells. *Circulation* 136, 1509–1524. <https://doi.org/10.1161/CIRCULATIONAHA.117.029003>.
123. Keys, H.R., and Knouse, K.A. (2022). Genome-scale CRISPR screening in a single mouse liver. *Cell Genomics* 2, 100217. <https://doi.org/10.1016/j.xgen.2022.100217>.
124. Shi, H., Li, Y., Xu, K., and Yin, J. (2023). Advantages of photo-curable collagen-based cell-laden bioinks compared to methacrylated gelatin (GelMA) in digital light processing (DLP) and extrusion bioprinting. *Mater. Today Bio* 23, 100799. <https://doi.org/10.1016/j.mtbio.2023.100799>.
125. Dunn, J.C.Y., Tompkins, R.G., and Yarmush, M.L. (1991). Long-term in vitro function of adult hepatocytes in a collagen sandwich configuration. *Biotechnol. Prog.* 7, 237–245. <https://doi.org/10.1021/bp00009a007>.
126. Seglen, P.O. (1976). Chapter 4. Preparation of Isolated Rat Liver Cells. *Methods Cell Biol.* 13, 29–83. [https://doi.org/10.1016/s0091-679x\(08\)61797-5](https://doi.org/10.1016/s0091-679x(08)61797-5).
127. Chen, A.A., Thomas, D.K., Ong, L.L., Schwartz, R.E., Golub, T.R., and Bhatia, S.N. (2011). Humanized mice with ectopic artificial liver tissues. *Proc. Natl. Acad. Sci. USA* 108, 11842–11847. <https://doi.org/10.1073/pnas.1101791108>.
128. March, S., Hui, E.E., Underhill, G.H., Khetani, S., and Bhatia, S.N. (2009). Microenvironmental regulation of the sinusoidal endothelial cell phenotype in vitro. *Hepatology* 50, 920–928. <https://doi.org/10.1002/hep.23085>.
129. Miller, J.S., Shen, C.J., Legant, W.R., Baranski, J.D., Blakely, B.L., and Chen, C.S. (2010). Bioactive hydrogels made from step-growth derived PEG-peptide macromers. *Biomaterials* 31, 3736–3743. <https://doi.org/10.1016/j.biomaterials.2010.01.058>.
130. Fairbanks, B.D., Schwartz, M.P., Bowman, C.N., and Anseth, K.S. (2009). Photoinitiated polymerization of PEG-diacrylate with lithium phenyl-2,4,6-trimethylbenzoylphosphinate: polymerization rate and cytocompatibility. *Biomaterials* 30, 6702–6707. <https://doi.org/10.1016/j.biomaterials.2009.08.055>.

STAR★METHODS

KEY RESOURCES TABLE

REAGENT or RESOURCE	SOURCE	IDENTIFIER
<b>Antibodies</b>		
CD31/PECAM-1 Antibody (JC/70A) [DyLight 550]	Novus	Cat# NB600-562R; RRID:AB_3195489
Alexa Fluor® 488 anti-mouse TER-119/Erythroid Cells Antibody	Biolegend	Cat# 116215; RRID:AB_493402
Cytokeratin 18 Monoclonal Antibody (DC10)	Thermo Fisher Scientific	Cat# MA5-12104; RRID:AB_10981680
Cytokeratin 19 antibody [EP1580Y]	Abcam	Cat# ab52625; RRID:AB_2281020
Anti- Arginase-1 antibody produced in rabbit	Sigma	Cat# HPA003595; RRID:AB_1078190
Goat Anti-Mouse E-cadherin Polyclonal antibody	R&D Systems	Cat# AF748; RRID:AB_355568
Anti-Vimentin antibody - Cytoskeleton Marker	Abcam	Cat# ab45939; RRID:AB_2257290
<b>Chemicals, peptides, and recombinant proteins</b>		
Gelatin from porcine skin, gel strength 300, Type A	Sigma-Aldrich	G2500
Methacrylic anhydride	Sigma-Aldrich	276685
PEGDA 3400 Da, powder	Allevi	SKU P3400-P-1
Lithium phenyl-2,4,6-trimethylbenzoylphosphinate	Sigma-Aldrich	900889
Tartrazine	Sigma-Aldrich	T0388
Phorbol 12-myristate 13-acetate	Sigma-Aldrich	P8139
eBioscience™ Lipopolysaccharide (LPS) Solution (500X)	Invitrogen	00-4976-93
Human IL-4 Recombinant Protein, PeptoTech®	Thermo Fisher Scientific	200-04
D-Luciferin, Potassium Salt	Gold Biotechnology	LUCK-100
Collagenase from Clostridium histolyticum	Sigma-Aldrich	C5138
Alexa Fluor™ 488 Phalloidin	Invitrogen	Cat# A12379
Hoechst 33342	Invitrogen	H3570
<b>Critical commercial assays</b>		
Enzyme-linked immunosorbent assay (ELISA)	Bethyl Laboratories	N/A
LIVE/DEAD™ Viability/Cytotoxicity Kit	Invitrogen	Cat# L3224
<b>Experimental models: Cell lines</b>		
Human: HUVECs, Passages 4 to 7	Lonza	C2519A
Human: NHDFs, Passages 4 to 10	Lonza	CC-2509
Human: MSCs, Passages 2-3	Lonza	PT-2501
Human: DPSCs, Passages 2-3	Lonza	PT-5025
Human: Primary hepatocytes	Gibco	Lot# 8357
Human: THP-1, Passages 2-3	Zheng et al. <sup>91</sup> ; Elizabeth Wayne Lab, University of Washington	N/A
Mouse: C57BL/6 Mouse Primary Dermal Fibroblasts - Adult	Cell Biologics	C57-6067
<b>Experimental models: Organisms/strains</b>		
Mouse: NCr nude, male and female, 8-12 weeks	Taconic Biosciences	N/A
Mouse: C57BL/6, female, 6-8 weeks	The Jackson Laboratory	N/A

(Continued on next page)

<b>Continued</b>		
REAGENT or RESOURCE	SOURCE	IDENTIFIER
Lentiviral vector expressing firefly luciferase under the albumin promoter (pTRIP.Alb.IVSb.IRES. tagRFP-DEST)	Andrus et al. <sup>109</sup> ; Charles Rice Lab, The Rockefeller University	N/A
Rat: Lewis, female, 4–8 weeks	Charles River Lab	N/A
<b>Software and algorithms</b>		
Auto CAD	Autodesk	<a href="https://www.autodesk.com/">https://www.autodesk.com/</a>
SolidWorks	SolidWorks	<a href="https://www.solidworks.com/">https://www.solidworks.com/</a>
Vesselucida 360	MBF BIOSCIENCE	<a href="https://www.mbfbioscience.com/">https://www.mbfbioscience.com/</a>
Vesselucida Explorer	MBF BIOSCIENCE	<a href="https://www.mbfbioscience.com/">https://www.mbfbioscience.com/</a>
JMP Pro	JMP	<a href="https://www.jmp.com/">https://www.jmp.com/</a>
GraphPad Prism	GraphPad	<a href="https://www.graphpad.com/">https://www.graphpad.com/</a>
R	The R Project for Statistical Computing	<a href="https://www.r-project.org/">https://www.r-project.org/</a>
Biorender	Biorender	<a href="https://app.biorender.com/">https://app.biorender.com/</a>

## EXPERIMENTAL MODEL AND STUDY PARTICIPANT DETAILS

### Animals

Male and female NCr nude mice aged 8–12 weeks old (Taconic Biosciences) and female C57BL/6 mice aged 6–8 weeks old (The Jackson Laboratory) were used in this study. All surgical procedures were conducted according to protocols approved by the University of Washington Animal Care and Use Committee.

### Primary cell cultures

Primary human umbilical vein endothelial cells (HUVECs; Lonza; passages 4 to 7) were cultured on dishes in EGM™-2 Endothelial Cell Growth Medium-2 BulletKit™ (EGM-2; Lonza). Normal human dermal fibroblasts (NHDFs; Lonza; passages 4 to 10) were cultured on dishes in Dulbecco's Modified Eagle's Medium (DMEM; Corning) with 10% (v/v) fetal bovine serum (FBS; Gibco) and 1% (v/v) penicillin-streptomycin (pen-strep; Invitrogen). Human mesenchymal stem cells (MSCs; Lonza; passages 2–3) were cultured in Mesenchymal Stem Cell Basal Medium supplemented with MSCGM SingleQuots (Lonza). Human dental pulp stem cells (DPSCs; Lonza; passages 2–3) were cultured in DMEM with Glutamax and 4.5g/L D-Glucose (Gibco), supplemented by 10% FBS (biowest), 1% nonessential amino acids (Gibco), 1% pen-strep (Invitrogen). Human hepatocytes (Gibco) were cultured in high-glucose DMEM (Corning) containing 10% (v/v) FBS (Gibco), 1% (v/v) insulin, transferrin, sodium selenite supplement (ITS; BD Biosciences), 7 ng/mL glucagon (Sigma), 0.04 ug/mL dexamethasone (Sigma), and 1% (v/v) pen-strep (Invitrogen). THP-1-STAT6-fluc cells (Wayne Lab) were subcultured in RPMI media (Gibco) containing 10% (v/v) FBS (Gibco) and 1% (v/v) pen-strep (Invitrogen). To be differentiated into macrophages, THP-1-STAT6-fluc cells were incubated with phorbol 12-myristate 13-acetate (PMA) for 48 h, followed by washing in cell culture media for 48 h. The macrophages are harvested by Accutase Cell Dissociation Reagent (Gibco) and plated or encapsulated for subsequent procedures as indicated. All cell cultures were at 37°C.

### Mouse and Rat Hepatocyte Isolation and Culture

Primary mouse and rat hepatocytes were isolated by *in situ* collagenase perfusion through the portal vein of a female C57BL/6 mouse (The Jackson Laboratory) and female Lewis rat (Charles River lab), respectively.<sup>125–128</sup> Hepatocyte culture media consisted of high glucose DMEM (Corning), 10% (v/v) FBS (Gibco), 1% (v/v) insulin, transferrin, sodium selenite supplement (ITS; BD Biosciences), 7 ng/mL glucagon (Sigma), 0.04 ug/mL dexamethasone (Sigma), and 1% (v/v) pen-strep (Invitrogen). Once isolated, primary mouse and rat hepatocytes were plated in AggreWell Micromolds (400µm square AggreWell micromolds, Stem Cell Technologies) along with NHDFs at a 1:1.6 ratio and incubated in hepatocyte culture media overnight at 37°C to form hepatic aggregates.<sup>32</sup>

## METHOD DETAILS

### Design of PHAST array architectures

Computer-aided design of PHAST array architectures was designed on SolidWorks (Dassault Systems SolidWorks Corp.) or AutoCAD (Autodesk).

### Polymer and photoinitiator synthesis

Poly(ethylene glycol) diacrylate (PEGDA, 3.4 kDa) was prepared as previously described<sup>129</sup> or purchased from Allevi. Lithium phenyl-2,4,6-trimethyl-benzoyl phosphinate (LAP) was synthesized as described previously<sup>130</sup> or purchased from Sigma.

Gelatin methacrylate (GelMA) was synthesized as previously described<sup>74</sup> with minor modifications.<sup>51</sup> Briefly, porcine gelatin (Sigma) was dissolved in carbonate-bicarbonate buffer at 50°C and methacrylic anhydride (Sigma) was added dropwise. After 3 h, the solution was precipitated with ethanol. The precipitate was allowed to dry, dissolved in phosphate-buffered saline (PBS, Fisher), and frozen at -80°C. The GelMA was then lyophilized and stored at -20°C until use.

### Material microenvironment synthesis and rheology characterization

GelMA infill materials were formulated to contain desired wt% GelMA (2, 3, 5, 7, 10, 12, 15, 20 wt%), 10 mM LAP, and PBS. Fibrin was prepared at 10 mg/mL from Fibrinogen (Bovine Plasma, Sigma) and Thrombin (Human plasma, Sigma). Type I collagen (Fisher) was prepared at 2 mg/mL. To investigate the mechanical properties of the material microenvironments screened in the PHAST array, we ran rheological measurements on all materials in bulk on an Anton Paar MCR-301 instrument equipped with a parallel-plate geometry (diameter = 8 mm) at a gap height of 500  $\mu\text{m}$ . First, we determined the proper frequency and amplitude (strain) for the materials to ensure we were in the linear viscoelastic range. We found that 5% strain and 0.5 Hz fell in that range for all samples tested. We then ran 6-minute time sweeps for all the conditions from 2-20 wt% GelMA and 10 mg/mL fibrin in triplicate. We pipetted 25  $\mu\text{L}$  of prepolymer directly onto the rheometer platform. The prepolymer was then equilibrated for 60 seconds, followed by a 30-second exposure of 405 nm light (Mightex BioLED, 24.5 mW/cm<sup>2</sup>) from the bottom of the custom-made, translucent plate to crosslink the gels. The storage (G') and loss (G'') moduli were allowed to stabilize with the remaining time, and the last thirty seconds of readings were averaged for the final storage modulus of the sample. All trials were conducted at room temperature.

### Fabrication and Handling of PHAST arrays

PHAST hydrogel arrays are printed using a custom-designed stereolithography apparatus for tissue engineering (SLATE) previously described.<sup>51</sup> PHAST arrays are printed under DLP light intensity of 24.5 mW cm<sup>-2</sup> using a mixture of 3.25:10 wt% 3.4 kDa PEGDA: GelMA, 17 mM LAP, and 1.519 mM tartrazine (Sigma) at 100  $\mu\text{m}$  layer thickness. PHAST arrays measure 18 mm x 18 mm x 2 mm. Each well is 1 mm deep and 1.5 mm in diameter. PHAST arrays are then rinsed to remove any unreacted monomer/tartrazine and allowed to swell to equilibrium for 3 days in PBS before further use.

The PHAST array is robust for handling with spatulas, which is how we typically transfer the device between incubation steps, filling, and surgical implantation procedures. If using forceps, flat or blunt forceps would be the preferred tool of choice for handling the device. Excessive force, such as crushing or extreme squeezing should be avoided when handling the device. The device can be securely sutured through a designated suture hole without fracturing, as long as the suture is left slightly loose and not pulled fully 'tight'; otherwise, it can cut through the device and/or cause a fracture.

### Filling of PHAST arrays

Materials screened in the PHAST array construct included any combination of Matrigel (Corning), collagen (Type I rat tail, Fisher), fibrin (10 mg/mL), 2, 3, 5, 7, 10, 12, 15, 20 wt% GelMA mixtures, or a hybrid material mixture of 1:1 10 mg/mL fibrin:5 wt% GelMA. For vascularization screening arrays, HUVECs and NHDFs were first washed with PBS to remove animal serum, detached with 0.25% trypsin solution (Corning), and spun into pellets corresponding to the number of conditions to be screened. For hepatic screening, hepatic aggregates were collected and spun into pellets corresponding to the number of conditions to be screened. All cell pellets were then resuspended into appropriate material. Cell density was calculated at 12,000 HUVECs/ $\mu\text{L}$ , 4,300-12,000 NHDFs/ $\mu\text{L}$ , 2,700 hepatocytes/ $\mu\text{L}$ , 10,000 THP-1-STAT6-fluc/ $\mu\text{L}$ .

To prepare PHAST arrays for cell seeding, wells within the array were carefully aspirated of PBS. The array was then positioned in an empty dish, and each well was seeded according to the "maps" created from the computational modeling and simulations (Figure S4). Each well received 1  $\mu\text{L}$  of material/cellular formulation. Prior to withdrawing of the solution to fill in the well, the cell-containing precursor solution was well mixed by the pipet to prevent cell from setting. This procedure was repeated prior to every withdrawing to allow uniform filling across the array. An electronic pipet was also used to provide highly accurate filling volume. After seeding a full array, the PHAST array was placed on the SLATE and allowed to photocrosslink the photoreactive (GelMA) moieties under near-UV (405 nm) light for 30 seconds. Constructs containing fibrin, Matrigel, or collagen moieties were allowed to additionally incubate at 37°C for 30 minutes before *in vitro* use or *in vivo* implantation.

### Cell viability within PHAST array

We tested the viability of both HUVECs and hepatic aggregates (primary rat hepatocytes and NHDFs) following seeding and photocrosslinking under 405 nm light for 30 seconds. Following light exposure, we incubated the cell-laden PHAST array hydrogels with LIVE/DEAD Viability/Cytotoxicity kit reagents (Invitrogen) according to manufacturer's instructions. Fluorescence imaging was performed on a confocal laser scanning microscope (Leica TCS SP8) in the Garvey Imaging Lab in the Institute for Stem Cells and Regenerative Medicine (ISCRM) at the University of Washington. A z-score map was generated by JMP Pro 17 software to evaluate the uniformity of initial number of living cells across the map.

### Fabrication of discrete engineered tissues for result validation

To validate the results obtained from PHAST arrays, we fabricated discrete engineered tissues 18 mm in diameter and 1 mm in thickness. The precursor solution containing cells were added to molds and photocrosslinked with the SLATE printer under violet light (405 nm) for 30 seconds.

### In vivo implantation of PHAST arrays and discrete tissues

All surgical procedures were conducted according to protocols approved by the University of Washington Animal Care and Use Committee. Male and female NCr nude mice aged 8–12 weeks old (Taconic) were anesthetized using isoflurane. PHAST array tissue constructs were sutured to the perigonadal fat pad through designated suture hole and positioned so that the open wells of the array were in direct apposition to the perigonadal fat pad. The beveled corner of the array was positioned in the top lefthand corner. The incisions were closed aseptically, and the animals were administered slow releasing buprenorphine (72 h) 1 mg/kg after surgery.

### PHAST array harvesting, processing, and immunohistochemistry

Mice were sacrificed at the termination of the experiment (7–14 days). Array constructs were harvested from the intraperitoneal space along with the engrafted perigonadal fat pad. The tissue constructs were immediately fixed following excision in 4% (v/v) paraformaldehyde (PFA; VWR) for 72 h at 4°C and then washed with PBS for 3 times, 30-minute durations.

To immunostain and visualize proteins of interest in 3D, thick tissue, we used an adapted version of the Clearing Enhanced 3D (Ce3D) method.<sup>77</sup> First, the excised array constructs were blocked whole overnight at room temperature in Ce3D alternative block buffer containing 1% (w/v) bovine serum albumin (BSA, Sigma), 1% (v/v) normal donkey serum (NDS; VWR), 0.1 M Tris (Sigma), and 0.3% (v/v) Triton X-100 (Sigma) with gentle shaking. The following day the tissues were incubated in primary antibody diluted 1:100 in fresh block buffer and 5% (v/v) dimethyl sulfoxide (DMSO; Sigma; a penetration enhancer) at 37°C for 24 h. Samples were washed for 6 h in fresh block buffer and incubated in species-appropriate, fluorophore-conjugated secondary antibody diluted 1:500 in fresh block buffer and 5% (v/v) DMSO overnight at 37°C with gentle shaking. Phalloidin (Invitrogen) was added 1:100 at this step to visualize actin cytoskeleton staining. Following this incubation, samples were washed for 6 h at room temperature in a wash buffer containing 0.2% (v/v) Triton X-100 and 0.5% (v/v) 1-thioglycerol (Sigma) in PBS with gentle shaking.

Immediately following immunostaining, we incubated samples in Ce3D clearing solution containing 22% (v/v) N-methylacetamide (Sigma), 80% (w/v) Histodenz (Sigma), 0.1% (v/v) Triton X-100 in PBS at room temperature for 24 h with gentle shaking. Hoechst 33342 (Invitrogen) was added 1:500 to the Ce3D solution to counterstain for nuclei. The arrays were then transferred to a larger volume of fresh Ce3D clearing solution the following day for long-term, light-protected storage at room temperature to enhance clearing.

The cleared array tissue constructs were placed on FluoroDish (World Precision Instrument) and 3D imaged on a confocal laser scanning microscope (Leica TCS SP8 or Nikon AX). Image z-stacks were acquired through Leica Application Suite X (LAS X) software (Leica Microsystems) or NIS-Element (Nikon).

To image an optically cleared PHAST array in its entirety, the 10x objective was used, and tiles of approximately 7 x 7 image stacks. Images were converted to Imaris image format (.ims) using Imaris File Converter 9.3.1 (Oxford Instruments), stitched using Imaris Stitcher 9.3.1 (Oxford Instruments) and visualized within Imaris 9.3.1 (Oxford Instruments) in 3D View or Slice Mode.

Image z-stacks of immunostained PHAST arrays were reconstructed in 3D using Vesselucida 360 software (MBF Bioscience). Vesselucida 360 was then used to generate parameterized data describing the architecture of the networks (volume, surface area, length). All analyses were performed blinded using Vesselucida Explorer software (MBF Bioscience) and then mapped back to the screened condition according to array maps.

### PHAST array map design

To engineer an array design that protects against “position effect” (i.e., the possibility that certain regions of the array promote better vascularization), we created a different array layout for each mouse. Each of the eight arrays shown in Figure S4 was designed such that each condition contained two technical replicates; furthermore, there were three technical replicates of the control. The arrays were designed so that the two replicates for a given condition were not within two rows of each other and were not the same number of columns away from the center column. Moreover, each subsequent array is a rotated version of the first one, shifted by a random number of rows and columns. Based on these conditions, colored array maps were generated using statistical computing software, R.

### Bioluminescent imaging

THP-1 cells were engineered to express red firefly luciferase under the signal transducer and activator of transcription 6 (STAT6) responsive elements as previously described.<sup>91</sup> The engineered THP-1-STAT6-fluc cells were differentiated to M0 macrophages by 24-h treatment of 10pg/μL phorbol 12-myristate 13-acetate (PMA) in RPMI 1640 medium supplemented by 10% FBS and 1% penicillin and streptomycin. Upon activation, THP-1-STAT6-fluc cells were incubated in cell culture media for at least 24 h before being harvested by StemPro™ Accutase™ Cell Dissociation Reagent (Thermo Fisher). For cells cultured in 2D, 10,000 cells per well were plated in 96 well plate and treated with 200 μL 100 pg/μL lipopolysaccharide (LPS; Invitrogen) or 40 pg/μL interleukin-4 (IL-4, PeproTech) for 48 h. For cells encapsulated in 3D, 10,000 cells/μL were mixed with prepolymer solution containing 5 wt% GelMA, 10mM LAP and cell culture media (N/A group), 100 pg/μL LPS (LPS group) or 40 pg/μL IL-4 (IL-4 group). 1μL prepolymer solution was added to 96 well plate or array as indicated in the map (Figure S5E) and crosslinked under violet light (405 nm) for 30 seconds. Crosslinked gel is then submerged in cell culture media. After 48 h *in vitro* culture, cells or gels were incubated with 150 μg/mL D-luciferin (GoldBio) prior to imaging using the In Vivo Imaging System (IVIS) Spectrum imaging system (PerkinElmer) and Average Radiance was quantified using Living Image software (PerkinElmer).

To visualize albumin-driven luciferase expression as an indirect metric for hepatic function, primary mouse, rat and human hepatocytes were transduced with a lentiviral vector expressing firefly luciferase under the albumin promoter (pTRIP.Alb.IVsb.IRES.tagRFP-DEST, provided through a Materials Transfer Agreement with Charles Rice, The Rockefeller University) as previously described.<sup>109</sup> The concentrated virus was diluted 1:5 in hepatocyte medium containing N-2-hydroxyethylpiperazine-N-2-ethane sulfonic acid buffer (HEPES; 20 mM; Gibco) and 4  $\mu\text{m}/\text{mL}$  polybrene (Sigma) in ultra-low attachments 6-well plates (Corning) for 6 h. After incubation, the transduced hepatocytes were collected for aggregating into hepatic aggregates and subsequent screening in PHAST arrays or as individual discrete liver tissues. After 1 week of implantation, arrays were explanted from the mouse host and immediately incubated with cell culture media containing D-luciferin (150  $\mu\text{g}/\text{mL}$ ; GoldBio) for 10 minutes and then imaged using IVIS. For mice carrying 3D printed discrete engineered liver tissues, 250  $\mu\text{L}$  15 mg/mL luciferin solution per mouse was injected intraperitoneally prior to imaging.

## 2D tissue histology

To process arrays for traditional 2D histology, previously fixed and tissue-cleared constructs were re-hydrated in PBS for 24 h. The arrays were then embedded in paraffin for immunohistochemical analysis. Arrays were sectioned in 5  $\mu\text{m}$  slices using a microtome and transferred to slides. For gross visualization of tissues within wells, sections were stained with hematoxylin and eosin (H&E).

Discrete engineered liver tissue was embedded in paraffin and sectioned in 10  $\mu\text{m}$  slices. Sections were stained for cytokeratin 18 and cytokeratin 19, arginase-1, or vimentin and imaged on a confocal laser scanning microscope (Nikon AX with NSPARC) with 40 x objective.

## Enzyme-Linked Immunosorbent Assay (ELISA)

For validation studies where we implanted engineered human liver tissue in mice, after a week of implantation, mice blood was retrieved via cardiac puncture and collected in clot-activating tube. The serum was separated by centrifugation at 1300 xg for 10 min and stored at  $-80^{\circ}\text{C}$  until measurement. Human albumin level in the serum was determined by ELISA (Bethyl Laboratories).

## QUANTIFICATION AND STATISTICAL ANALYSIS

### Linear models to account for mouse, condition, position, and crosstalk

Let  $\text{vol}_{ijk}$  denote the vessel volume (huCD31<sup>+</sup>) for a well in mouse  $i$  that received condition  $j$  and is located in position  $k$ . Let  $\widehat{\text{vol}}_{ijk}$  be the predicted percent vessel for a well in mouse  $i$  with condition  $j$  in position  $k$ . We first fit a model of the form

$$\log(\widehat{\text{vol}}_{ijk}) = \beta_{\text{mouse } i} + \beta_{\text{cond } j},$$

where we refer to  $\beta_{\text{mouse } i}$  as the mouse effect and  $\beta_{\text{cond } j}$  as the condition effect. To obtain the p-values displayed [Figure 3E](#), we tested the null hypothesis that the fixed effect for a given experimental condition without NHDFs equals the fixed effect for the same condition with NHDFs added. In this section, we focus on vessel volume measured with CD31, but similar models fit for each of the other dependent variables displayed in [Figure 3E](#).

To obtain the eight residual maps shown in [Figure S7](#), we computed the values of  $\log(\text{vol}_{ijk}) - \log(\widehat{\text{vol}}_{ijk})$  for every position in every mouse. The ‘Average’ residual map in [Figure S7](#) shows the values of  $\log(\text{vol}_{ijk}) - \log(\widehat{\text{vol}}_{ijk})$  for each position averaged across mice. These residuals show leftover variation in log vessel volume after accounting for mouse and condition. Any consistent pattern across mice in these residual plots would provide evidence of a position effect. [Figure S7](#) does not clearly provide such evidence.

Despite the lack of clear visual evidence of a position effect ([Figure S7A](#)), we conducted a formal statistical test for the presence of a position effect. Our model imposed left-right symmetry on the coefficients corresponding to the positions. Furthermore, we modeled the position effect as monotone from the top to the bottom of the array. The model is as follows:

$$\log(\widehat{\text{vol}}_{ijk}) = \beta_{\text{mouse } i} + \beta_{\text{cond } j} + \beta_{\text{row}} \cdot \text{row}_k + \beta_{\text{col}} \cdot |\text{column}_k - 4|.$$

In this model,  $\text{row}_k$  denotes the row corresponding to position  $k$  and  $\text{col}_k$  denotes the column corresponding to position  $k$  (each range from 1 to 7). When we fit this model, neither  $\beta_{\text{row}}$  nor  $\beta_{\text{column}}$  were found to be statistically significantly different from 0.

Finally, to consider the possibility of spatial correlation, or ‘‘crosstalk’’, across the array, we conducted a Moran’s I-test to test the null hypothesis that neighboring wells of the array have independent residuals in models fit to volume, surface area, and length of the HuCD31<sup>+</sup> vessels ([Figure S7B](#)). Large p-values mean that there is no strong evidence of spatial dependence in the residuals.

## Power analysis

For each number of mice ranging from 2-21, we generated 1000 synthetic datasets. Each synthetic dataset uses arrays designed according to the layout in [Figure S4A](#). Let  $\text{pva}_{ijk}$  denote the percent vessel area for a well in mouse  $i$  with condition  $j$  in position  $k$ . The synthetic datasets are generated from the following model:

$$\text{pva}_{ijk} = \beta_{\text{mouse } i} + \beta_{\text{cond } j} + \beta_{\text{row}} \cdot \text{row}_k + \beta_{\text{col}} \cdot |\text{column}_k - 4| + \epsilon_{ijk}.$$

The magnitudes of the row effect, column distance effect, mouse effects, and noise ( $\epsilon_{ijk}$ ) match that of the initial PHAST data ([Figure 2](#)). In the synthetic datasets, fourteen conditions have no effect, meaning that their average percent vessel area matches

that of the control condition. Seven of the conditions (the active conditions) have an average vessel volume that is 25 percentage points higher than the control condition. This assumed effect size is smaller than the difference between 5 wt% GelMA and 15 wt % GelMA microenvironments in the initial PHAST data (Figure 2).

After generating each synthetic data set, we fit a linear model that accounts for mouse, row effect and column distance effect, and condition effect. The estimated power is the proportion of times, across all datasets and across all active conditions, that we observe a statistically significant effect at  $\alpha=0.05$  with a Bonferroni correction for multiple comparisons. The estimated power, as a function of the number of mice, is shown in Figure S4B. This simulation study shows that we can achieve greater than 90% power to detect a 25 percentage point difference in vessel volume using as few as eight mice.

### Statistical analysis

All data are represented as mean  $\pm$  SEM. One-way analysis of variance (ANOVA) followed by Tukey's post-hoc test or Mann-Whitney test were conducted as indicated in texts.